# Modeling of Large Deformations of Hyperelastic Materials

E. Boudaia[#1], L. Bousshine[*2]

[#] Department of Mechanical Engineering, Faculty of Science and Technology,

BP 523, Mghrila, 23000 Béni Mellal, Morocco

[*]Laboratoire des Technologies de Constructions et des Systèmes Industriels, ENSEM,

 BP 8118, Oasis, Casablanca, Morocco

[1]boudelhassan@yahoo.fr, [2]lbousshine@ yahoo.fr

*Abstract*

The elastomer properties (large deformations, damping) make their use more and more common in industries such as aerospace, automotive, construction and civil engineering or even the entertainment industry... Modeling the behavior of such materials is highly nonlinear, the nonlinearities are both geometric (due to large deformations imposed) and behavioral (behavior laws used are nonlinear). This paper presents a detailed description of the numerical implementation of incompressible isotropic hyperelastic behavior. In this study, the analysis of large deformation problems of Ogden's hyperelastic is based on the finite element method (FEM) and mathematical programming. To solve the problem of balance, we suggest using the combined Newton-Raphson/Arc-length procedure. A typical example is presented to illustrate the performance of this formulation.

*Keywords*

*Elastomers; Hyperelasticity; Large Strain; FEM; Newton-Raphson Algorithm; Arc-Length Scheme*

## Introduction

The theoretical studies of hyperelastic materials have mobilized many researchers for decades; see eg the work of Treloar [1], Gent [2] and Frakley [3]. However, the first important works were proposed by Mooney [4] and Rivlin [5]. Valani and al. [6] proposed to write the strain energy in a form separated following the main directions. This led to the widely used model of Ogden [7, 8]. Recently, different models have been developed for hyperelastic materials especially in biomechanics (Zulliger and al. [9]).

The objective of this paper is to present the model most widely used hyperelastic behavior and in particular the isotropic model. To do this, the different results of basic mechanics of the major changes are outlined in the first place. Are recalled and the various tensor quantities used in the modeling of continuous medium and medium formulation based on isotropic hyperelastic tensor structure. In a second step, the most widely used hyperelastic potential is exposed.

## Description of Large Strains

Elastomers, with hyperelastic behavior, usually work in large strains. Note $\vec{x}$ and $\vec{X}$ positions vectors of a particle P of a deformable body in the current configuration (where the solid occupies the volume $\Omega$ ) and initial (where the solid occupies the volume $\Omega_0$ ). We will use the same reference $(o, \vec{e}_1, \vec{e}_2, \vec{e}_3)$ for the initial configuration $C_0$ given at time $t_0$ and deformed configuration $C_t$ at time $t$ (Fig.1).
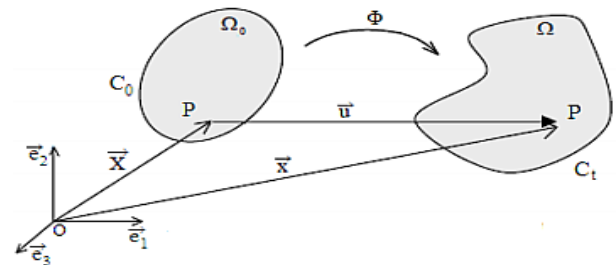


FIG. 1 INITIAL AND DEFORMED CONFIGURATIONS

For a Lagrangian description, the movement of the body can be defined relative to a reference configuration $C_0$, by a vector function:

$$\Phi : \begin{cases} C_0 \rightarrow C_t \\ \vec{X} \mapsto \vec{x} = \Phi(\vec{X}, t). \end{cases} \qquad (1)$$

By introducing the displacement vector $\vec{u}$ and we write the equation (1) in the equivalent form:

$$\vec{x} = \vec{X} + \vec{u}(\vec{X}, t). \qquad (2)$$

Order to describe the geometric transformations associated with these large strains, we introduce the deformation gradient tensor $F$ defined by:

$$F_{ij}(\vec{X},t) = \frac{\partial \Phi_i(\vec{X},t)}{\partial X_j} = \frac{\partial x_i}{\partial X_j} = \delta_{ij} + \frac{\partial u_i}{\partial X_j}, \tag{3}$$

Where

$\delta_{ij}$ denotes the Kronecker symbol.

Or equation (3) can be written in matrix form:

$$F = I + \nabla u, \tag{4}$$

Where

$I$ is the unit tensor,

$\nabla$ is the gradient tensor of displacements.

Due to the large displacements and large rotations, the strain tensor of Green-Lagrange $E$ was adopted to describe the nonlinear relationship between the deformation and displacement:

$$E = \frac{1}{2}(C - I), \tag{5}$$

Where

$C = F^T F$ is the strain tensor of Cauchy-Green right.

In the case of a hyperelastic law, there is a strain energy density $W$ which depends on one of the strain tensor and whose derivative gives the second stress tensor of Piola-Kirchhoff $S$:

$$S_{ij} = \frac{\partial W}{\partial E_{ij}} = 2\frac{\partial W}{\partial C_{ij}}. \tag{6}$$

In the particular case of isotropic hyperelasticity [10], equation (6) can be written as follows:

$$S = 2\left[ I_3 \frac{\partial W}{\partial I_3} C^{-1} + \left( \frac{\partial W}{\partial I_1} + I_1 \frac{\partial W}{\partial I_2} \right) - \frac{\partial W}{\partial I_2} C \right], \tag{7}$$

Where

$I_i$ ($i = 1, 2, 3$) are the invariants of the Cauchy-Green tensor on the right, $C$, such as:

$$I_1 = tr(C) ; \quad I_2 = \frac{1}{2}\left[ I_1^2 - tr(C^2) \right] \text{ and } I_3 = \det(C), \tag{8}$$

Where

$tr(\bullet)$ and $\det(\bullet)$ indicate, respectively, the trace and the determinant of a tensor.

Note that $S$ has no physical meaning but it is symmetric and purely Lagrangian, and from which one can determine the expression of the Cauchy tensor $\sigma$ :

$$\sigma = \frac{1}{\det(F)} FSF^T. \tag{9}$$

For the Ogden model [7] for incompressible materials, the energy density is expressed in terms of eigenvalues $\lambda_j$ ($j = 1, 2, 3$) of the Cauchy-Green tensor right by:

$$W(\lambda_1, \lambda_2, \lambda_3) = \sum_k^m \frac{\mu_k}{\alpha_k}\left( \lambda_1^{\alpha_k} + \lambda_2^{\alpha_k} + \lambda_3^{\alpha_k} - 3 \right), \tag{10}$$

where the constants are the material parameters and m is the total strain energy terms.

We recall that the incompressibility of the material results in $\det(F) = 1$ ou $\lambda_1 \lambda_2 \lambda_3 = 1$. Hence, the energy density can be expressed only by $\lambda_1$ and $\lambda_2$ :

$$W(\lambda_1, \lambda_2, \lambda_3) = \sum_k^m \frac{\mu_k}{\alpha_k}\left( \lambda_1^{\alpha_k} + \lambda_2^{\alpha_k} + \frac{1}{\lambda_1^{\alpha_k} \lambda_2^{\alpha_k}} - 3 \right). \tag{11}$$

## Variational Formulation

Solving the problem balance of incompressible hyperelastic is reduced to problem of minimizing the functional $\Psi$ :

$$\begin{cases} Min \quad \left[ \Psi(u,S) = \int_\Omega \left( S.E(u) - \overline{f}.u \right)d\Omega - \int_{\Gamma_t} \overline{t}.ud\Gamma \right] \\ Subject \ to \begin{bmatrix} Conditions \ of \ incompressibility, \\ Boundary \ conditions \ (u = \overline{u} \ on \ \Gamma_u). \end{bmatrix} \end{cases} \tag{12}$$

Where

$\Omega$ is an isotropic structure, subject to surface forces $\overline{t}$ on the surface $\Gamma_t$,

$\overline{f}$ is the gravity forces,

$\overline{u}$ is displacements imposed on the surface $\Gamma_u$ .

The nonlinear equations (12) are solved numerically with the finite element method whose the approximation of the displacement field is defined by the relation:

$$u(x) = N(x)U \text{ with } \varepsilon = \nabla(N(x))U, \tag{13}$$

Where

$x = < x, y, z >$ are the nodal coordinates,

$N(x)$ is the shape functions matrix,

$U$ is the vector of unknown nodal displacements.

Therefore, the functional $\Psi$ takes the discretized form as follows:

$$\Psi(U) = \int_{\Omega} \Big( S.E(N.U) - N^T.\overline{f}.U \Big) d\Omega - \int_{\Gamma_t} N^T.\overline{t}.U d\Gamma. \qquad (14)$$

Thus, the discrete system (14) can be solved iteratively by using the combined Newton-Raphson/Arc-length procedure (see [11] for details on the implementation of this method in the context finite element).

## Numerical Example

In this example, we consider a plate with a central circular hole in the stress plane and tension is sought under a constant displacement up to 100% elongation. Geometry (L × D = 25.4 × 14.24 cm²) with a unit thickness is shown in Fig. 2. For more details see reference [12]. Due to symmetry of geometry, only one quarter of the plate is modeled, as shown below.
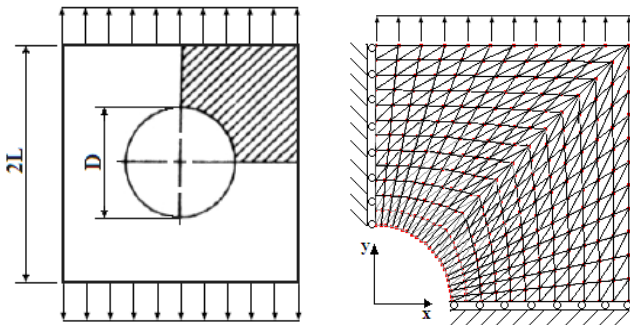


FIG. 2 GEOMETRY AND LOADING (LEFT) AND BOUNDARY CONDITIONS WITH MESHES (528 ELEMENTS T3) (RIGHT)
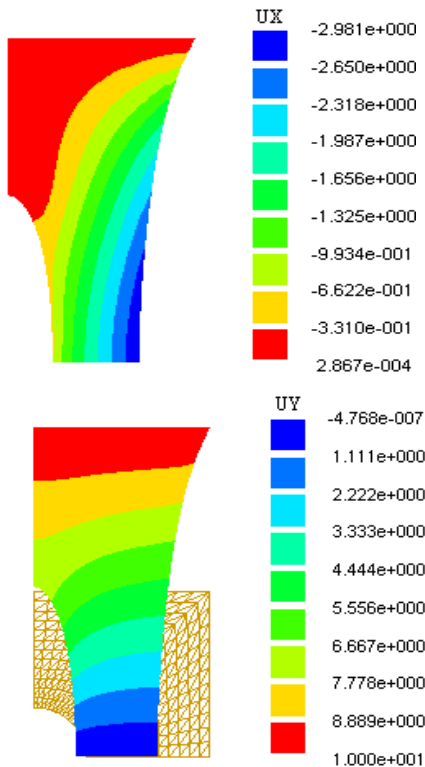


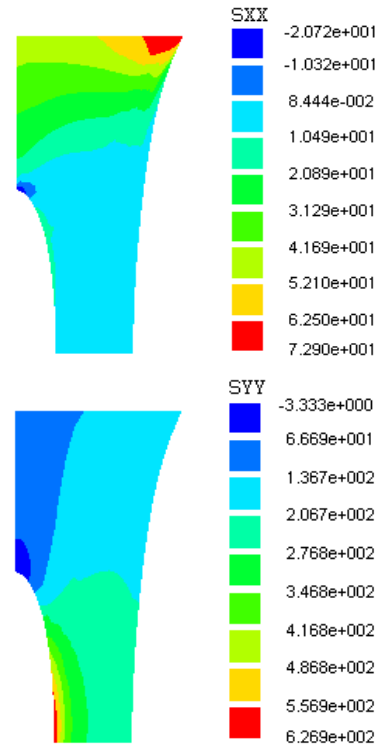FIG. 3 DEFORMATION ALONG THE X AXIS (TOP) AND ALONG THE Y AXIS (BELOW).



FIG. 4 ISOVALUES OF STRESS ALONG THE X AXIS (TOP) AND ALONG THE Y AXIS (BELOW).

## Conclusions

A computational method by using the mathematical programming and the analysis approach hyperelastic is developed here to investigate the large deformation. A finite element model in conjunction with the combined Newton - Raphson / Arc - length procedure was adopted allowing investigating interesting applications. The obtained results illustrate the effectiveness of our approach developed.

This work can be extended in the future by taking into account other parameters as frictional contact with heat transfer.

### REFERENCES

[1] L. R. G. Treloar, The Physics of Rubber Elasticity. 3rd edition, Oxford university press, 1975.

[2] N. Gent, "Rubber and Rubber Elasticity, a Review." Journal of Polymer Science: Polymer Symposia, vol. 48, pp. 1–17, 1974.

[3] P. K. Frakley and A. R. Payne, Theory and Practice of Enginnering with Rubber. Applied Science Publishers, London, 1978.

[4] M. Mooney, "A Theory of Large Elastic Deformations." Journal of Applied Mechanics, vol. 11, pp. 582–592, 1940.

[5] R. S. Rivlin, "Large elastic Deformations of Isotropic Materials IV." Further developments of the general theory, Philosophical Transactions of the Royal Society of London, Series A, vol. 24, pp. 1379–397, 1948.

[6] K. C. Valanis and R. F. Landel, "The Strain-Energy Function of a Hyperelastic Material in Terms of the Extension Ratios." Journal of Applied Physics, vol. 38, pp. 2997–3002, 1967.

[7] R. W. Ogden, "Large Deformation Isotropic Elastic - on the Correlation of Theory and Experiment for Incompressible Rubberlike Solids." Proceedings of the Royal Society A, vol. 326, 565–584, 1972.

[8] R.W. Ogden, "Elastic Deformation of Rubber-Like Solids." The Rondey Hill 60th Anniversary Volume, Editor: H.G. Hopkins and M.J. Sewell, Pergamon, Oxford, 1982.

[9] M. A. Zulliger, P. Fridez, K. Hayashi and N. Stergiopulos, "A Strain Energy Function for Arteries Accounting For Wall Composition and Structure." Journal of Biomechanics, vol. 37, 989–1000, 2004.

[10] F. Peyraut, Z. Q. Feng and N. Labed, "A Material-Independent Algorithm for Preserving of the Orientation of the Spatial Basis Attached to Deforming Medium." Comput. Mech. Vol. 21, 1053-1060, 2007.

[11] E. S. Neto, D. Perié and D. R. J. Owen, Computational Methods for Plasticity: Theory and Applications. John Wiley & Sons Ltd, 2008.

[12] E. A. Neto De Souza. Perlc Djordje and D. R. J. Owen, "Finite Elasticity In Spatial Description: Linearization Aspects with 3-D Membrane Applications." Inter. J. For Num. Meth. In Eng., vol. 38, 3365-3381, 1995.

**El Hassan Boudaia** is an associate Professor at the Mechanical Engineering Department of Faculty of Science and Technology of Beni Mellal, Morocco. His Ph.D thesis in 2007 was on the subject of a meshless and finite element methods analysis for elasto-plastic contact problems with friction. His current research activities are multidisciplinary and focus mainly on design approaches and reliability analysis, especially in structural engineering. Using the elasto-plastic analysis and the meshless or the finite element method, he has published with his coworkers many works on the reliability assessment of structures, especially in the non-associated elasto-plasticity area.

# New Approach to Durability of Glassceramic and Silicate Glass

Volodymyr P. Maslov

V.Ye. Lashkarev Institute of Semiconductor Physics, National Academy of Sciences of Ukraine, 41, prospect Nauky, Kyiv, 03028 Ukraine

maslov@isp.kiev.ua

*Abstract*

The goal of this work is to determine correlation of amorphous nonmetallic materials with defective surface layers and their physical properties. Microcreep processes in tested materials can be described by general equation that is known as logarithmic microcreep equation. Applicability of this equation for tested optical materials is indicative for microcreep processes in crystalline and amorphous hard materials. For each grade of polished optical glass, minimal residual defective layer exists. Parameters of this layer are interrelated with mechanical properties of glassceramics and glass, such as microhardness and optical strain coefficient, and thermophysical properties, such as thermal diffusivity, sintering temperature, and annealing temperature. It is first suggested to estimate durability of optical silicate glass and glassceramic, using $E \cdot a^{1/2}$ parameter (E -elasticity modulus, a - thermal diffusivity).

*Keywords*

*Defective Layer; Microcreep; Durability; Glassceramic; Glass*

## Introduction

The structure and behavior of surface layers of crystals under external mechanical actions were analyzed by Alekhin in [1]. Using silicon and germanium single crystals as test samples, he found the common regularity of the surface microplasticity, which consists in the fact that at the initial loading stages the gradient distribution of dislocations within the near-surface sample layers, up to several tens of micrometers in thickness, takes place. The study using a low-energy electron diffraction [2, 3] showed that atoms of crystal surface layers were essentially displaced relative to their normal positions in the crystal lattice due to the asymmetry of interatomic forces. Therefore, complex two-dimensional structures having other lattice symmetry, density, length and type of interatomic bonds are formed in the crystal surface layers. The special features of the lattice dynamics and the variations of the lattice

thermodynamic functions are responsible for the higher deformation ability of the crystal surface layers and increased velocity of dislocation movement. Crystal surface layers are characterized by the decreased Pierls-Nabarro barriers and a higher activation volume. The surface vacancies contribute to the decrease of the Pierls-Nabarro barriers, making much easier the dislocation movement. Brittle cracks in crystalline materials initiate due to the non-uniformity of the microdeformation in the near-surface layers.

The above studies were not performed for amorphous nonmetallic hard materials. The purpose of this work was using silicate optical glass as an example, to relate the strength of brittle amorphous nonmetallic materials to the parameters of their surface layers and the material physical properties.

## Results

The analysis of the effect of the surface state on the microcreep of optical glassceramics, fused quartz, and certain silicate glass like K8, BK10, TK14, and LK6 has shown that even at room temperature the microcreep is recorded. The studies were carried out on a high-sensitive device for the registration of a relative elongation ($\varepsilon$) of the samples measuring 50 x 5 x 0.6 mm. The relative elongation was calculated by the Chebyshev formula [4]

$$\varepsilon = \frac{\Delta l}{l_0} = \frac{8}{3}\left(\frac{\lambda_0 - \lambda_1}{l_0^2}\right), \qquad (1)$$

where $\lambda_0$ is the deflection of a foil indicator applied to the sample before loading, $\lambda_1$ is the deflection of the indicator after the loading.

The maximal microcreep rate was exhibited by the samples ground with abrasive material M28. The minimal microcreep rate and the residual strain were observed for the samples with distorted surface layers

removed by mechanical polishing or chemical etching by a hydrofluoric acid solution. The kinetics of the microcreep of the studied materials may be found using the following general equation:

$$\varepsilon = \frac{\Delta l}{l_0} = \alpha \cdot \ln \tau + \beta, \qquad (2)$$

The coefficients $\alpha$ and $\beta$ for the studied optical materials are given in Table 1.

TABLE 1 THE COEFFICIENTS A AND B FOR THE STUDIED OPTICAL MATERIALS

| Material | Treatment | $\alpha, 10^6$ | $\beta, 10^5$ |
|---|---|---|---|
| Quartz glass | Chemical etching in hydrofluoric acid solution | 3.6 | -1.0 |
| | Mechanical polishing | 5.5 | -0.6 |
| | Grinding with abrasive material M10 | 6.7 | 0.4 |
| | Grinding with abrasive material M28 | 7.5 | 1.4 |
| Optical glassceramics CO115M | Chemical etching in hydrofluoric acid solution | 3.8 | -0.3 |
| | Mechanical polishing | 4.8 | 0.5 |
| | Grinding with abrasive material M10 | 6.5 | 1.0 |
| | Grinding with abrasive material M28 | 8.7 | 1.8 |
| Silicate glass as K8, BK10, TK14, and LK6 | Chemical etching in hydrofluoric acid solution | 3.5 | -0.2 |
| | Mechanical polishing | 3.0 | 0.3 |
| | Grinding with abrasive material M10 | 10.0 | 0.5 |
| | Grinding with abrasive material M28 | 12.0 | 1.1 |

Note:

1. Average grain sizes of M10 and M28 abrasive materials are 10 and 28 μm, respectively.

2. CO115M (Russian analogue of Zerodur - glassceramics with coefficient of thermal expansion equal zero) is thermoresistant nano-filled glass-ceramics.

Equation (2) is known as the equation that describes logarithmic microcreep of metals and alloys. The applicability of this equation to tested optical materials indicates that microcreep processes are common to crystalline and noncrystalline hard materials. The possibility of the existence of structural microdiscontinuities like dislocations in noncrystalline materials is discussed in [5, 6].

The experimental results obtained in tension studies [4] give grounds to suggest that there is a set of local sources of displacement of interatomic bonds in the studied materials. The concentration of the local sources depends on the preceding machining of the material surface. Under the action of external mechanical stresses, these sources are gradually included in the common microdeformation process until the saturation state is achieved. For this reason, the saturation state in material samples with a thick distorted layer is achieved at the large values of relative elongation. The presence of the distorted surface layer increases the amount of near-surface defects, which are displaced under the action of the constant external load and thermal fluctuations, reducing the elasticity of the surface layer.

The removal of the distorted layer reduces the relative elongation of the sample approximately by a factor of 2, when using mechanical polishing, and by a factor of 1.5 − 6, when using chemical etching in hydrofluoric acid solution, as compared to the initial ground samples.

It has been established that the product of the strength ($\sigma$) by the relative elongation ($\varepsilon$) of a sample at creeping is constant for a specified temperature and material [7, 8]. The physical meaning of this parameter is defined as the external force work on microdeformation that is required for the destruction of a unit volume of the material. If this work is constant for each material and does not depend on the condition of the material surface, the strength of the material sample after grinding ($\sigma_g$) may be determined by the strength of the polished material sample ($\sigma_0$):

$$\sigma_g = \sigma_0 \frac{\varepsilon_0}{\varepsilon_g}. \qquad (3)$$

where $\varepsilon_0$ is the relative elongation of the polished sample, and $\varepsilon_g$ is the relative elongation of the ground sample at steady creeping.

Of theoretical and practical interest is to consider the interrelation between the parameters of the polished surface condition of the optical glass sample and the physical properties of the glass.

For the analysis, samples of optical glasses of commercial grades were used, such as flint glass TF10, TF7, TF1, and BF28 and crown glass BK10, STK3, TK23, K8, and LK7. The physical properties of these

materials are given in GOST 13659-78 "Optical colorless glass - Physical and chemical properties - Basic parameters" (USSR State Standard).

Previously it was proposed [9-13] to use ellipsometric parameters of substances, specifically the minimal ellipticity, to describe the parameters characterizing the condition of the distorted surface layer of crystalline, amorphous, or glassceramics. The ellipsometric parameters are ellipticity (tgρ) and phase difference (Δ) between the $p$ and $s$ components of the electric field vector of the optical wave reflected from the glass sample surface. The values of these parameters are defined by the light and material interaction.

For isotropic dielectrics, the intensity of the $p$ component of the electric field vector at a Brewster angle ($\varphi_B$) and the ellipticity (tgρ) are zero, and the phase difference (Δ) changes from π (if $\varphi < \varphi_B$) to 0 (if $\varphi > \varphi_B$).

The reason for the use of this method is the fact that the mechanical grinding and polishing of the surface bring about the initiation of brittle cracks and deformation of interatomic bonds in the material, thus reducing the refraction coefficient and change the minimal ellipticity of the material. All the surface layers with microcracks (a relief layer, a fractured layer, and a layer with deformed structure) are characterized by deformed and dangling interatomic bonds. The distribution of defects in the distorted layer may be analyzed by layer-by-layer removing each distorted layer by polishing and measuring the minimal ellipticity at each stage of the removal.

A typical experimental relation of the change of the ellipticity in layer-by-layer removal of distorted layers by polishing may be written by Eq. (4)

$$\text{tgρ} = (\text{tgρ}_0 - \text{tgρ}_{\min})e^{-bx}, \qquad (4)$$

where $tgρ_0$ is the ellipticity of the polished surface with maximal distortions, $tgρ_{min}$ is the minimal ellipticity after removing all distorted layers by polishing, $b$ is constant for the given material, and $x$ is the distance from the treated surface.

The found dependence of the distribution of defects in a distorted layer and a comparison of our data with the results [14] allow us to represent the material machining as a continuous process of the defect accumulation in the near-surface layer, which results in the separation of worn out particles from the surface machined.

The interaction of abrasive grains with the glass surface in machining can be presented as a combination of the indentation of abrasive grains into the material, scratching of the material surface, and initiation of brittle microcracks. According to [15], the propagation of a brittle microcrack in a glass is accompanied with the generation of thermal energy at a distance of several tens of Angstrom unit from the tip of a microcrack. As a result, the temperature within this area increases up to the glass sintering temperature (several hundred degrees C). So, the formation of the distorted layer is accompanied with the temperature changes induced by nonstationary local thermal processes that coincide with the thermal diffusivity of the workpiece material in physical meaning.

Of interest is to relate the experimental values of the distorted layer parameter $tgρ$ to the thermal diffusivity of the workpiece material. For this purpose, a physical model was proposed, according to which the distribution of distortions in the surface layer is identical to the distribution of thermal energy needed to transfer it into the bulk of the material [16]. For this reason, the thermal diffusivity of the material can be used as a parameter characterizing the process of the material machining.

The experimental data show that, for each glass grade, the minimal residual ellipticity ($tgρ_{min}$) remains even after thorough (deep) polishing of the glass surface. A comparison of $tgρ_{min}$ for each glass grade with the glass physical properties has made it possible to determine the dependence of this parameter on the mechanical properties of glass, like microhardness (H) and optical strain coefficient (B), and on thermophysical properties, such as thermal diffusivity (a), sintering temperature ($T_s$), and annealing temperature ($T_a$). The greater are the values of these properties, the less is the value of the parameter $tgρ_{min}$ (see Fig.1–3).
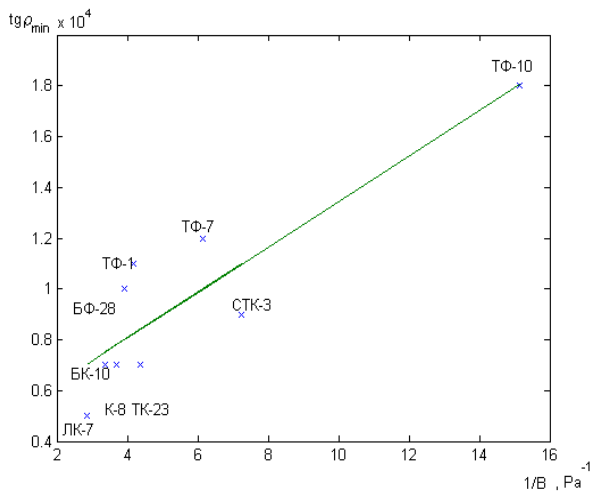
As can be seen from Fig. 1–3, the mechanical and thermophysical properties of the studied material affect the formation and parameters of the distorted surface layer. It may be suggested that the polished surface layer is an analog of the zone with deformation of interatomic bonds at the tip of a crack in the material (see Fig. 4).
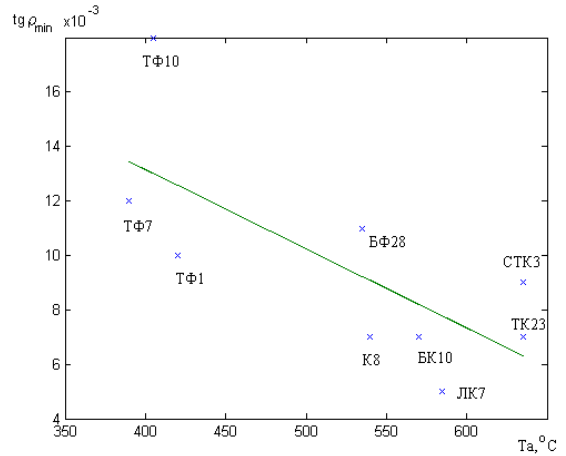
(a)
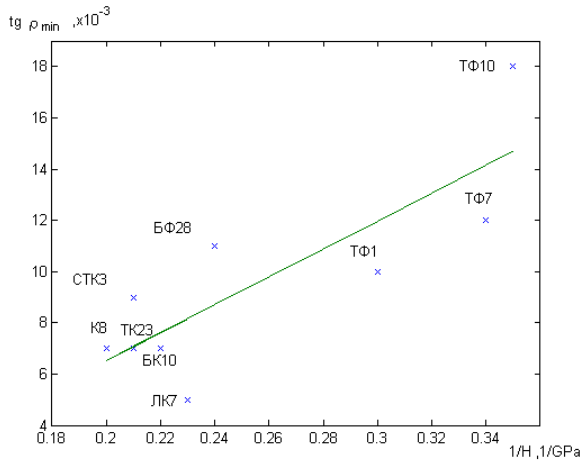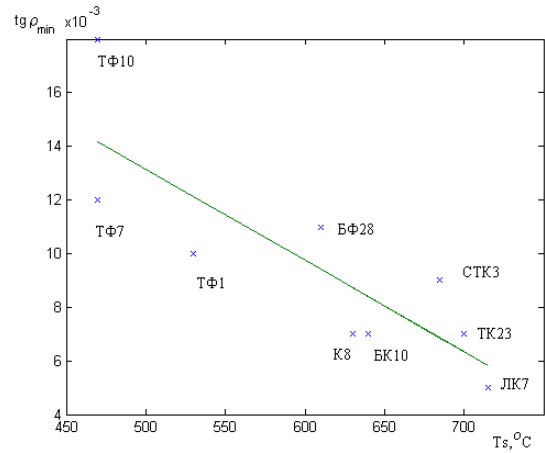


(b)

FIG. 1 MINIMAL ELLIPTICITY FOR A POLISHED SURFACE OF OPTICAL GLASS VS. MICROHARDNESS (A) AND THE OPTICAL STRAIN COEFFICIENT (B)



(a)



(b)

FIG. 3 MINIMAL ELLIPTICITY FOR A POLISHED SURFACE OF OPTICAL GLASS VS. SINTERING (A), AND ANNEALING (B) TEMPERATURE OF THE GLASS
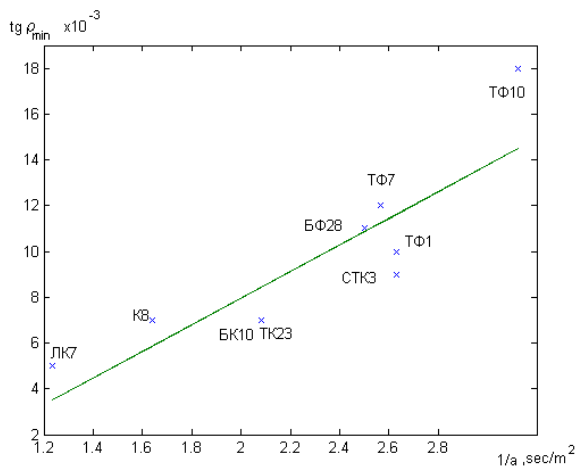


FIG. 2 MINIMAL ELLIPTICITY FOR A POLISHED SURFACE OF OPTICAL GLASS AS A FUNCTION THE THERMAL DIFFUSIVITY OF THE GLASS
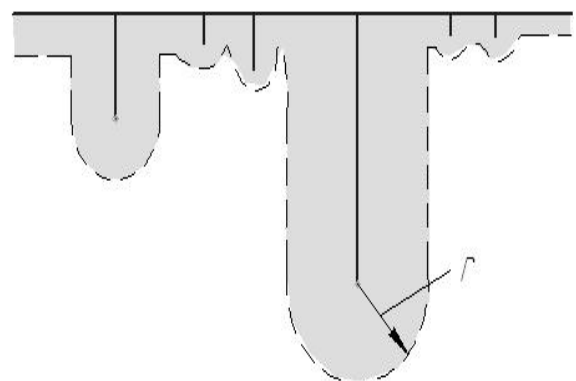


FIG. 4 SCHEMATIC OF THE DISTORTED SURFACE LAYER STRUCTURE WITH MICROCRACKS AFTER MECHANICAL POLISHING ($R$ IS THE RADIUS OF THE DEFORMATION ZONE WITH DANGLING INTERATOMIC BONDS AT THE TIP OF A CRACK)

Fig. 5 illustrates the microstructure of the polished surface of the Zerodur glass ceramics after chemical etching, which supports the schematic shown in Fig. 4.
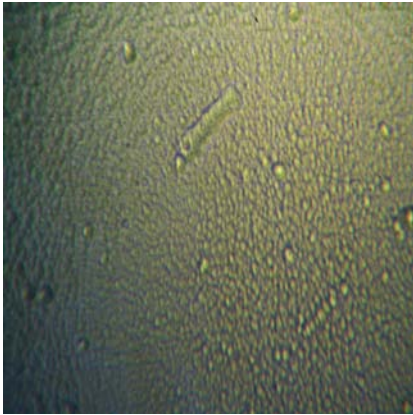


FIG. 5 MICROSTRUCTURE OF THE POLISHED SURFACE OF THE ZERODUR GLASSCERAMICS SAMPLE AFTER CHEMICAL ETCHING (X600)

## Discussion

The radius (r) of the deformation zone with dangling interatomic bonds at the tip of a crack can be expressed in terms of the parameter $tg_{Qmin}$:

$$r = k \cdot tg\ _{Qmin} = k \cdot 1/a, \tag{5}$$

where k is the coefficient of proportionality, $a = 1/tg\ _{Qmin}$ is the thermal diffusivity of the material.

According to Griffiths [17] and Inglis 18], the strength of brittle materials can be determined as follows:

$$\sigma = (8 E\gamma / \pi\, r)^{1/2}, \tag{6}$$

where E is the elasticity modulus, $\gamma$ is the specific surface energy.

Taking into consideration (5) and the fact that the specific surface energy is proportional to the elasticity modulus, equation (6) can be expressed as follows:

$$\sigma = A \cdot E \cdot a^{1/2}, \tag{7}$$

where A is the coefficient of proportionality.

The values of the thermal diffusivity of the material can be found in reference book or calculated by the following equation:

$$a = \lambda / C_P d, \tag{8}$$

where $\lambda$ is the thermal conductivity, $C_P$ is the specific heat capacity, and $d$ is the density of the material.

Fig. 6 shows the durability values for 23 grades of optical glass as a function of the parameter $E \cdot a^{1/2}$. The durability values were taken from [19], and the elasticity modulus values were taken from GOST 13659-78.
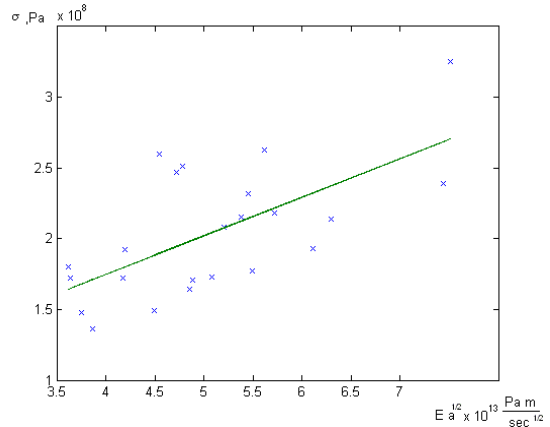


FIG. 6  DURABILITY VALUES OF SILICATE GLASSES AS A FUNCTION OF THE E·A$^{1/2}$ PARAMETER.

The coefficient of proportionality A can be determined from Fig. 6 as follows:

$$\sigma_x = 4\ (E\ a^{1/2})_x,\ \text{Мпа}, \tag{9}$$

where index $x$ designates the corresponding to unknown glass.

The use of Eq. (9) provides a possibility to determine the strength of most known of silicate glass with an error of no more than 30 %.

## Conclusions

The microcreep processes in glass or glassceramics can be described by a general equation that is known as the logarithmic microcreep equation. The applicability of this equation for studied optical materials is indicative for microcreep processes in crystalline and amorphous hard materials.

A minimal residual distorted layer exists for polished optical glass and glassceramics. These layer parameters depend on mechanical (microhardness and optical strain coefficient) and thermophysical (thermal diffusivity, sintering and annealing temperature) properties of glass.

It is first suggested to estimate durability of optical silicate glass and glassceramic, using $E\, a^{1/2}$ parameter (E -elasticity modulus, a - thermal diffusivity)

## REFERENCES

[1]  Alekhin V.P., Physics of Strength and Plasticity of Surface Layers of Materials; M., Nauka, 1983, 280.

[2]  Mac Rae A.U., The Use of Thin Films in Physical Investigation; England, 1966, Pt. 2, 98-102.

[3] Lander I.I., Progress in solid-state chemistry; NY, Pergamon Press, 1965, Vol.2, 26-38.

[4] Dvorskii A.A., Maslov V. P., Novikov V.N., Effect of the State of a Surface on the Microcreep of Optical Glass Ceramic, fused quartz, and Certain Silicate Glass, such as Crown Glass, at a Room Temperature; Strength Problems, 1987, 91-94.

[5] Gilman J.J., Unified Viewpoint on Deformation in Materials; M., Metallurgiia, 1972, 7-18.

[6] P.Chandhari, A.Zevi, P. Steindhardt, Edge and other Dislocations in Amorphous Solids; Phys. Rev. Lett., 1979, Vol. 43, No. 20, 1517-1520.

[7] Dvorskii A.A., Maslov V. P., Method for Determining the Strength of Fragile Nonmetallic Materials, USSR Application No. 1211629, Bulletin 6, 1986, 192.

[8] Dvorskii A.A., Maslov V. P., Novikov V.N., Interrelation between the Strength and Microflow of Surface Layersn of Optical Glass Ceramic SO115M, Fused Quartz Glass, and Silicate Glass K8, Strength Problems, 1988, No. 4, 118-119.

[9] Maslov V. P., Melnyk T.S., Skachkov M.M., Scherbakov L.E., Analysis of the State of the Surface Layer of Glass Ceramic after Mechanical Treatment; OMP, 1978, No. 8, 70-71.

[10] Vladimirova T.V., Gorban N.Y., Maslov V. P., Melnyk T.S., Odarych V.A., Analysis of the Optical Properties and Structure of the Surface Layer of Glass Ceramics, OMP, 1979, No. 9, 31-34.

[11] Maslov V. P., Melnyk T.S., Odarych V.A., Ellipsometric Analysis of the Surface of Crystalline Quartz after Mechanical Treatment; OMP, 1985, No. 4, 1-2.

[12] Gorydko N.Y., Maslov V. P., Novikov V.N., Sergiienko E.A., Analysis of the Depth of the Surface Layers of LiF and CdSb Crystals Damaged by Mechanical Treatment; OMP, 1980, No. 9, 13-15.

[13] Gorydko N.Y., Maslov V. P., Novikov V.N., Shvydkyi V.A., Topography of Near-Surface Defects of Quartz Monocrystals, OMP, 1980, No. 10,. 32-33.

[14] Tsesnek L.S., Mechanics and Microphysics of Abrasion of Surfaces; M., Mashinostroieniie, 1979, 264.

[15] Hilling V.B., Plasticity and Destruction of Glass; Microplasticity, M., Metallurgiia, 1972, 315-338.

[16] Maslov V. P., Chumachkova M.M., A Physical Model of the Formation of a Surface Layer Broken by Mechanical Treatment in Materials for Optical-Electronic and Sensor Devices, Ukr. J. Phys, 2008, V 53, No. 10, 978-982.

[17] Griffith A.A., Phil.Trans. Roy-Soc., London, 1921, Vol. A221, 163.

[18] Inglis C.E., Trans. Inst. Naval. Arch., 1913, Vol. 55, 219.

[19] Ivanov A.V., Strength of Optical materials; L., Mashinostroieniie, 1984, 144.

**Volodymyr P. Maslov** graduated from the Moscow Engineering Physics Institute (MEPhI, State University) in 1969. From 1974 to 2000, he worked in the enterprises of optical industry. Since 2001 he has been working as a senior researcher, and since 2011 - as a head of department of science of sensory materials at the Institute of Semiconductor Physics of the National Academy of Sciences of Ukraine. He received his PhD degree in 1973 and Dr.Sc.(Techn.) in 2008. He is professor of NTUU KPI. His scientific interests are optical engineering and mechanical behavior of functional materials.

# Phase Formation through a Stage of Liquid State in Metallic Materials Being Electrodeposited: Recent Experimental Proofs

Oleg B. Girin

Department of Materials Science, Ukrainian State University of Chemical Technology, Prospekt Gagarina 8, Dnipropetrovsk 49005, Ukraine

girin@ua.fm

## Abstract

The effect of increase of density of metals being electrodeposited under the influence of a centrifugal force acting perpendicular to the crystallization front is found. Wave-like flow of surface layers of metals being electrodeposited under the influence of a centrifugal force acting parallel to the crystallization front, as well as bending of waves by mechanical hindrances and formation of foam on the crests of waves are discovered. Change of form of the deposits of metals being electrodeposited under the influence of a centrifugal force including the growth of length and thickness of the deposits at the direction of force action with a modification of their configuration depending on overload values is discovered. Predominant development of deposits of metals being electrodeposited beyond the edge of the cathode in the direction of the action of a centrifugal force parallel to the crystallization front is found. The obtained results prove the validity of the discovered phenomenon of phase formation through a stage of liquid state in metallic materials being electrodeposited.

## Keywords

*Phase Formation; Electrodeposited Metal; Liquid State; Centrifugal Force; Density; Surface Morphology*

## Introduction

The phenomenon of phase formation through a stage of liquid state in metallic materials being electrodeposited was theoretically predicted in 1986 [1] and in 1988 it was experimentally found [2]. The essence of the discovered phenomenon is that during the electrochemical deposition of a metallic material onto a solid cathode in an aqueous medium a supercooled metallic liquid is being formed and solidified at the deposition temperature in the form of a crystalline or/and an amorphous phase.

In the work [3] it is shown that liquid state of a metallic material being electrodeposited is caused by very quick (explosive) character of its formation as a result of chain reaction of electrochemical formation of atoms. At that during one act of explosive growth 40-60 atoms are being formed on average. With regard to very quick passage of the act of explosive growth (about $10^{-7}$ sec), the atoms have no time to form a structure with long-distance order of their arrangement. Multitude of such clusters of atoms are being formed in avalanche-like manner in various places on the surface of the cathode or the growing deposit and then being combined into larger formations constitute liquid phase of a metallic material being electrodeposited.

The two aspects should be mentioned. First, a liquid being formed during electrodeposition of a metallic material is always supercooled. Second, a liquid of a metallic material being electrodeposited is consequence of its high-energy but not a high-temperature state as in conventional melts.

During recent years many experimental results proving the validity of this phenomenon were obtained [4-9]. The goal of this work was the further experimental proof of the validity of the discovered phenomenon.

## Experimental Proof of Validity of the Phenomenon

### Idea One and Its Realization

It is known that during the centrifuging of a liquid metallic material due to the action of a centrifugal force it presses itself to the walls of a rotating mould, becomes denser and crystallizes in a more compact ingot (so called centrifugal casting). Therefore, if during electrocrystallization a metallic material really passes through a stage of liquid state, then as a result

of a centrifugal force acting perpendicular to the crystallization front it should be expected the formation of an electrodeposit, which is denser in comparison with an electrodeposit obtained under ordinary conditions.

For the obtaining of metals being electrodeposited in the field of a centrifugal force, the unit was developed and constructed [10]. The unit provided the action of a centrifugal force proportional to the normal acceleration $kg$ (where $k$ – overload coefficient) ranging from 1 $g$ to 1256 $g$. The values of a centrifugal force was changed stepwise by varying the number of rotations of the centrifuge rotor from 0 to 3000 rotations per minute with the step of 500, which resulted in the normal acceleration of 1 $g$, 35 $g$, 140 $g$, 314 $g$, 558 $g$, 872 $g$ and 1256 $g$. The unit allowed influencing by a centrifugal force on a metal being electrodeposited both perpendicular and parallel to the crystallization front depending on the electrodes positions in the electrochemical cell.

Construction features of the centrifuge and the electrochemical cells completely eliminated a possibility of electrolyte flow relatively to the cathode during electrodeposition of metals [10]. During the operation of centrifuge the cells rotated horizontally jointly with the rotor. The cathode was mounted on the bottom of the cell perpendicular to its axis, thus during rotation of the cell the cathode was perpendicular to the rotor radius. As a centrifugal force during rotation is always directed along with the rotor radius from its center, such position of the cathode provided force influence on a metal is electrodeposited perpendicular to the crystallization front.

In order to eliminate the influence of hydrogen on the density of deposits being formed in the field of a centrifugal force, the investigations were performed on samples of copper and nickel being electrodeposited with the current yield values of 99.5-100 % (Table 1).

The duration of obtaining of each sample was 60 min. In order to avoid the reduction of concentration of metal ions in the electrolytes during electrodeposition, the soluble anodes were used. Density of copper and nickel electrodeposits was determined by the method of hydrostatic weighing.

As a result of the completed investigations, it was found that the influence of a centrifugal force on metals was electrodeposited perpendicular to the crystallization front causes increase of their density (Fig. 1).

TABLE I ELECTROLYTES COMPOSITION AND PARAMETERS OF DEPOSITION OF METALS IN THE FIELD OF CENTRIFUGAL FORCE

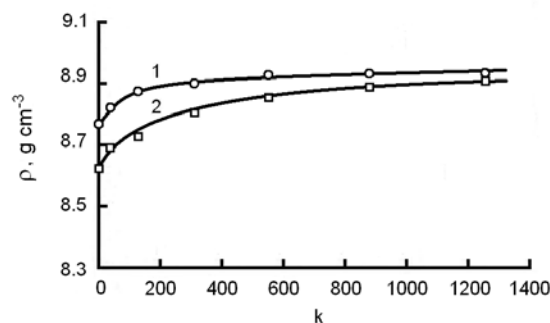| Metal | Electrolytes Composition, g L$^{-1}$ | Electrolyte Temperature, °C | Current Density, A dm$^{-2}$ | Current Yield, % |
|---|---|---|---|---|
| Cu | $CuSO_4 \cdot 5H_2O$ – 250 $H_2SO_4$ – 50 | 25 | 1 | 100 |
| Ni | $NiSO_4 \cdot 7H_2O$ – 330 $NiCl_2 \cdot 6H_2O$ – 50 $H_3BO_3$ – 35 $C_{11}H_{23}COONa$ – 0.1 | 25 | 1 | 99.5 |



FIG. 1 CHANGE OF DENSITY OF COPPER (1) AND NICKEL (2) BEING ELECTRODEPOSITED DEPENDING ON THE OVERLOAD COEFFICIENT

Character of the influence of the overload on the density of the investigated metals is the same: growth of $k$ value up to 314 cause's significant increase of density and subsequent growth of $k$ value up to 1256 results in minor increase of density of metals. The most abrupt increase of metals density (from 8.76 to 8.88 g cm$^{-3}$ for copper and from 8.62 to 8.72 g cm$^{-3}$ for nickel) was found during low overloads (under $k$ = 139).

The obtained result can be explained by tightening of a liquid phase being formed during electrochemical deposition of metals. A possibility of obtaining of more dense metals by their electrodeposition in the field of a centrifugal force in comparison with metals obtained under ordinary conditions indicates that metals during electrochemical deposition really pass through a stage of liquid state.

Thus, the found effect of increase of density of metals being electrodeposited under the influence of a

centrifugal force directed perpendicular to the crystallization front confirms the validity of the discussed phenomenon.

### Idea Two and Its Realization

It is known that a liquid metallic material in contrast to a solid one is able to flow i.e. to move its mass in the direction of action of the applied force. Therefore if a metallic material during electrochemical deposition really passes through a stage of liquid state, then under the influence of a centrifugal force parallel to the crystallization front it should be expected the movement of its mass by the wave-like flow of continuously replenishing liquid surface layers. Indeed, the force influence on the continuously forming liquid surface layers of a material being electrodeposited will cause oscillating motion of liquid surface which in turn will result in formation of waves.

The investigations were performed on samples of nickel and copper electrodeposited in the field of a centrifugal force. The cathode was mounted in the cell parallel to its axis, therefore during the rotation of the cell, the cathode was parallel to the rotor radius which provided force influence on a metal being electrodeposited parallel to the crystallization front. Due to the metal current yield values 99.5-100% and impossibility of electrolyte motion relative to the cathode in the cell during electrodeposition [10], the influence of hydrogen and electrolyte motion on surface morphology were completely eliminated.

As a result of the completed investigations, the effect of wave-like flow of surface layers of metals being electrodeposited in the direction of action of a centrifugal force was found. The most obviously solidified waves were fixed on the surface of nickel electrodeposits obtained at the force influence proportional to 1256 $g$ (Fig. 2).

Thus at the absence of a centrifugal force the surface of nickel deposits is smooth and does not contain wave-like forms (Fig. 2 a), but as a result of significant overload the surface of deposits of nickel being electrodeposited contains solidified waves (Figs. 2 b-d). Such surface morphology is a result of solidification of surface layers of nickel being electrodeposited which are in liquid state and participate in wave-like motion under the influence of a centrifugal force parallel to the crystallization front.
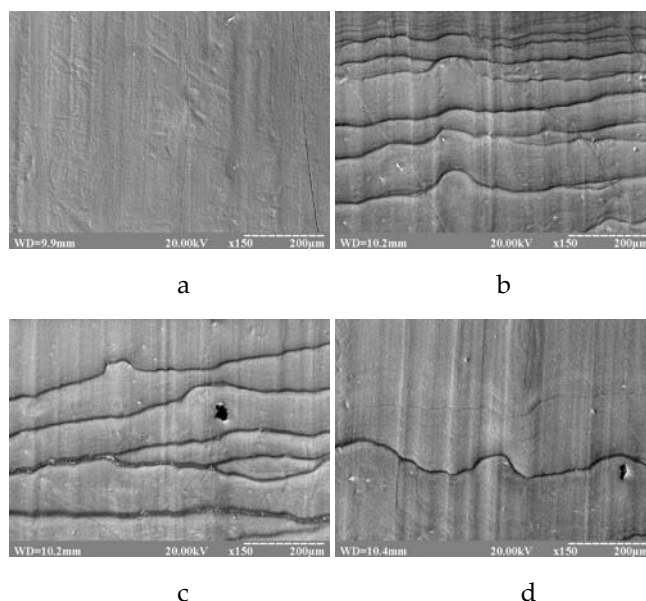


a

b

c

d

FIG. 2 SCANNING ELECTRON MICROSCOPY IMAGES OF NICKEL ELECTRODEPOSITS DEMONSTRATING WAVE-LIKE FLOW OF SURFACE LAYERS OF NICKEL BEING ELECTRODEPOSITED UNDER THE INFLUENCE OF A CENTRIFUGAL FORCE PROPORTIONAL TO ACCELERATION OF 1 $G$ (A – INITIAL CONDITION) AND 1256 $G$ (B-D) THE FORCE IS DIRECTED FROM TOP TO BOTTOM

There are two main features of wave-like flow of surface layers of metals being electrodeposited. First, metallic waves are bent by macroscopic defects such as solid inclusions (Fig. 2 b) or through pores (Figs. 2 c, d). Such bending of waves by mechanical hindrances is typical for a liquid material with high viscosity. Assume that a material being electrodeposited is in solid state only (e.g. as fine solid particles), then in that case pores would be filled with particles and there would be cavities around solid inclusions caused by curl-like motion of particles.

In Fig. 3, typical images of metallic waves bent by a through pore and by a solid inclusion as well as structure of waves nearby the mentioned hindrances are presented. As it is seen in Fig. 3, wave-like areas of material have a form of semicircular terraces and contain particles of a globular form which are seemingly solidified clusters or groups of clusters of a material.

Another typical feature proving the origin of wave-like forms from solidification of metallic liquid moving under the influence of a centrifugal force is the formation of foam on the crests of waves. Thus in Figs. 3 a, b the areas of solidified foam formed on the crests of waves as a result of mechanical dispersion of metallic liquid under force influence are seen.
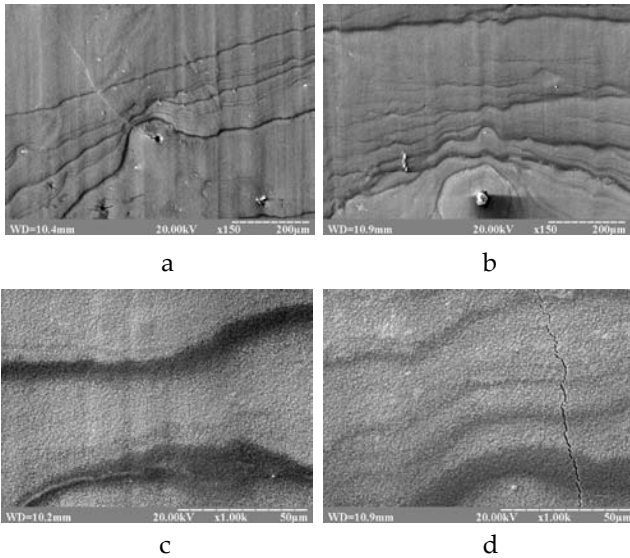
FIG. 3 SCANNING ELECTRON MICROSCOPY IMAGES OF NICKEL ELECTRODEPOSITS SHOWING WAVES BENT BY A PORE (A,C) AND BY AN INCLUSION (B,D) THE FORCE PROPORTIONAL TO ACCELERATION OF 1256*G* IS DIRECTED FROM TOP TO BOTTOM

As at minor values of a centrifugal force solidified waves have wide crests, the morphology of foam areas was investigated on the samples of nickel deposits obtained at minor force influence (proportional to 35 *g* and 140 *g*). As it is seen in Fig. 4 solidified foam is glassy formations of various configurations poorly adhered to the base. Thus in Figs. 4 a, b, the areas of the crests of waves of nickel deposits with partially peeled off fragments of solidified foam as a result of its cracking are clearly seen. The layer of glassy foam is thin enough for coating structure to be seen through it (Figs. 4 c, d).
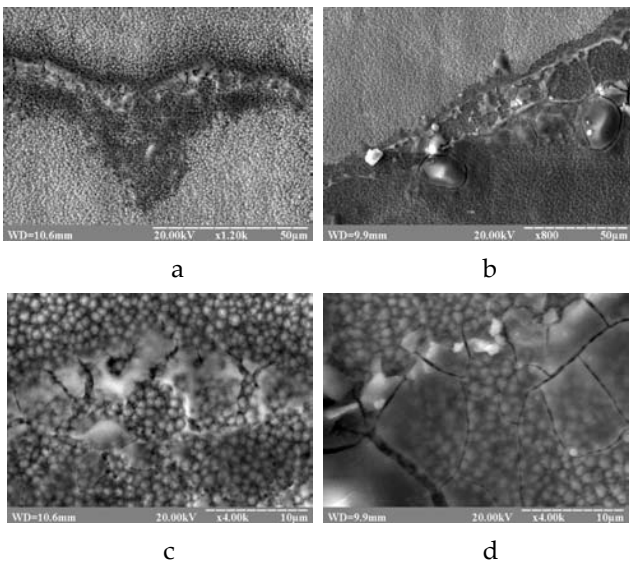


FIG. 4 SCANNING ELECTRON MICROSCOPY IMAGES OF NICKEL ELECTRODEPOSITS WITH FRAGMENTS OF SOLIDIFIED FOAM ON THE CRESTS OF WAVES THE FORCE PROPORTIONAL TO ACCELERATION OF 35*G* (A,C) AND 140*G* (B,D) IS DIRECTED FROM TOP TO BOTTOM

Fig. 4 clearly proves the existence of foam formed during wave-like flow of liquid surface layer of nickel being electrodeposited and frozen as a result of its very quick solidification. Indeed, assume that wave-like flow of surface layer of a metal being electrodeposited under the influence of a centrifugal force is caused by the movement of fine solid particles, then after the end of the process the foam should not exist and a metal should be not in a monolithic but in a powder form.

The differences in configurations of metallic waves of electrodeposited copper and nickel under the influence of a centrifugal force are caused by coarse structure of copper. At the same time, the main features of past liquid state retain. The first one is wave-like flow of its surface layers, the second one is bending of waves by mechanical hindrances (large globules and their groups) and the third one is the appearance of solidified foam on the crests of waves.

One of the results proving the validity of the discussed phenomenon is a wave-like area of solidified foam found on surface of a copper electrodeposit (Fig. 5 a). The various fragments of this foam wave area shown in Figs. 5 b-d clearly demonstrate the consequences of passing through a stage of liquid state by copper being electrodeposited.

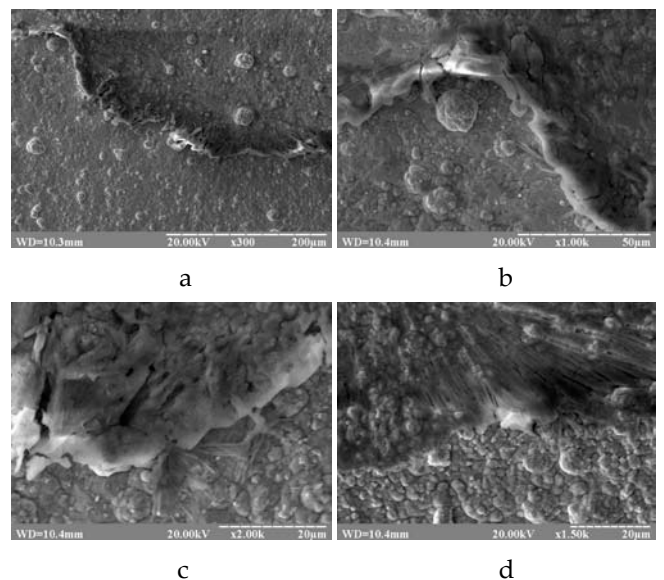Thus, wave-like flow of surface layers of metals being electrodeposited under the influence of a centrifugal



FIG. 5 SCANNING ELECTRON MICROSCOPY IMAGES OF COPPER ELECTRODEPOSIT DEMONSTRATING SOLIDIFIED WAVE-LIKE FOAM (A) AND FRAGMENTS OF ITS VARIOUS AREAS (B-D) THE FORCE PROPORTIONAL TO ACCELERATION OF 314*G* IS DIRECTED FROM TOP TO BOTTOM

force acting parallel to the crystallization front as well as bending of waves by mechanical hindrances and formation of foam on the crests of waves prove the validity of the discovered phenomenon.

### Idea Three and Its Realization

It is known that a metallic material in liquid state in contrast to a material in solid state possesses very low shear strength. Hence, a liquid metallic material is principally different from a solid one by its ability to change its form under the influence of an acting force. Therefore, if during electrochemical deposition a metallic material really passes through a stage of liquid state, then under the influence of a centrifugal force acting parallel to the crystallization front it should be expected a change of form of the deposit in the direction of the force action. Indeed, as a result of the solidification of the metallic liquid, shifted relative to the cathode, increase of length and thickness of the deposit as well as change of its configuration in the direction of an acting force are quite probable.

For the realization of this idea, a change of form of deposits of copper and nickel being electrodeposited under the influence of a centrifugal force acting parallel to the crystallization front was investigated. The cathode was mounted in the cell parallel to its axis, therefore during rotation of the cell the cathode was parallel to the rotor radius, which provided force influence on a metal being electrodeposited parallel to the crystallization front.

Thin plates of nickel (for copper deposition) and copper (for nickel deposition) were used as the cathode. Due to current yield of a metal of 99.5%~100 % and impossibility of electrolyte motion relative to the cathode in the cell during electrodeposition [10] the influence of hydrogen formation and electrolyte motion on a form of metal deposits was completely eliminated. A change of form of deposits of metals being electrodeposited was controlled by comparison of electron microscopy images of the far edge of deposits in the direction of action of a centrifugal force.

As a result of the completed investigations, it was found a change of form of the deposits of metals being electrodeposited under the influence of a centrifugal force acting parallel to the crystallization front (Fig. 6). Thus under usual electrodeposition conditions, i.e. when the rotor is at rest ($k = 1$), the far edge of copper electrodeposit was level and somewhat curved to the cathode surface (Fig. 6a). With an increase of overload

to $k = 35$ the far edge of the deposit became thicker and this bulge had a form of spherical segment along the edge of the cathode (Fig. 6 b).
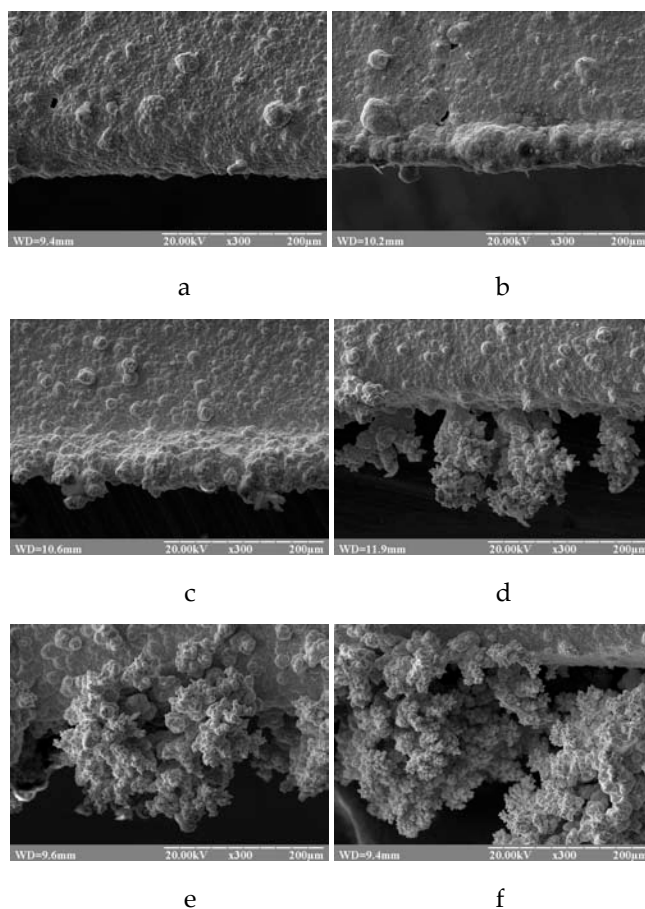


a          b

c          d

e          f

FIG. 6 SCANNING ELECTRON MICROSCOPY IMAGES OF THE FAR EDGE OF COPPER DEPOSITS ILLUSTRATING A CHANGE OF THEIR FORM DURING ELECTRODEPOSITION UNDER THE INFLUENCE OF A CENTRIFUGAL FORCE PROPORTIONAL TO ACCELERATION OF 1 $G$ (A) – INITIAL CONDITION, 35 $G$ (B), 140 $G$ (C), 558 $G$ (D), 872 $G$ (E) AND 1256 $G$ (F) THE FORCE IS DIRECTED FROM TOP TO BOTTOM

The observed change of form of copper deposit is explained by the fact that forming clusters of copper being electrodeposited and being in liquid state or their formations move toward the edge of the cathode under the influence of a centrifugal force. Adhesion force of copper clusters being solidified and the cathode (or an already solidified deposit area) seemingly is greater than the value of a centrifugal force. Therefore the influence of a minor centrifugal force, directed parallel to the crystallization front, on a metal being electrodeposited causes mainly thickening of a deposit edge.

The further increase of overload to $k = 140$ causes deformation of the bulge edge of a deposit in the direction of action of the force and formation of

evident deposit areas going beyond the edge of the cathode (Fig. 6 c). Drastic change of form of the copper deposit occurs after the increase of overload to $k = 558$ (Fig. 6 d). At this overload botryoidal deposit areas appear beyond the edge of the cathode in the direction of the action of the force.

The obtained form of the deposit is explained by the fact that at $k = 558$ a centrifugal force is seemingly greater than adhesion force of copper clusters being solidified and the cathode (or already solidified area of the deposit). As a result of the influence on copper, during its electrodeposition by a centrifugal force of a significant value parallel to the crystallization front, the essential shift of continuously replenishing liquid copper clusters or their formations relative to the deposit surface occurs. Solidification of continuously forming liquid phase being under force influence causes both the development of already existing deposit areas beyond the edge of the cathode and the formation of new areas.

The concept of metals being electrodeposited passing through a stage of liquid state is clearly proved by the further change of form of deposits of copper being electrodeposited with the increase of a centrifugal force. As it is seen in Fig. 6 e, the increase of force influence to the overload of $k = 872$ on copper being electrodeposited results in growth and branching of the deposit areas going beyond the edge of the cathode.

The results of an experiment on the influence of a centrifugal force proportional to acceleration of 1256 $g$ on copper being electrodeposited are especially impressive. Fig. 6 f indicates that the far edge of copper deposit in the direction of such force influence changed its form fundamentally relative to the initial one (Fig. 6 a). Thus the edge of copper deposit contains grown dendrite areas going far beyond the edge of the cathode both in the direction of the action of the force and in the other directions (Fig. 6 f).

The analysis of morphology of deposit areas going beyond the edge of the cathode in the direction of the action of the force (Fig. 7) shows that under minor overload ($k = 35$) these areas consist of solidified half-round drops formed by many fine globular clusters formations (Fig. 7, a).

With the increase of overload to $k = 140$ globular form of the deposit surface retains but the areas going beyond the edge of the cathode obtain elongated form. The further increase of overload to $k = 314$ causes

formation of more branched and relief areas of copper being electrodeposited beyond the edge of the cathode (Fig. 7 b). At overloads of $k = 558$ and 872 the size of particles of the areas decreases, they become flattened and gain more differentiated structure (Fig. 7 c).
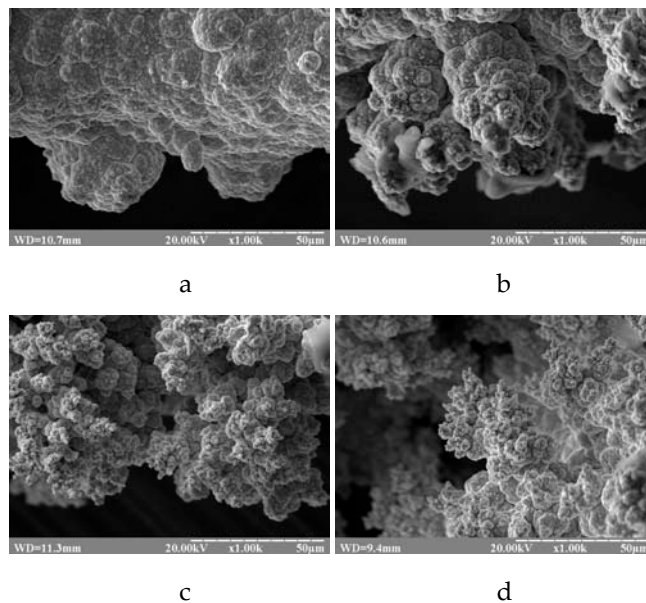


FIG. 7 SCANNING ELECTRON MICROSCOPY IMAGES OF THE FAR EDGE OF COPPER DEPOSITS SHOWING MORPHOLOGY OF THE AREAS GOING BEYOND THE EDGE OF THE CATHODE DEPOSITS WERE OBTAINED BY ELECTRODEPOSITION UNDER FORCE INFLUENCE PROPORTIONAL TO ACCELERATION OF 35 $G$ (A), 314 $G$ (B), 872 $G$ (C) AND 1256 $G$ (D). THE FORCE IS DIRECTED FROM TOP TO BOTTOM.

Electrodeposition of copper at great force overloads ($k = 1256$) results in fundamental change of morphology of deposit areas going beyond the edge of the cathode. The size of particles of these areas decreases significantly, they gain disk-like and spindle-like forms, their growth occurs in various directions. Thus in the center of Fig. 7 d, it is shown a deposit area beyond the edge of the cathode developing towards force influence.

The found effect of form change of deposits of copper being electrodeposited under the influence of a centrifugal force is completely proved by the analysis of the far edge of nickel deposits obtained under various force influences during their electrodeposition (Fig. 8). According to the obtained results, force influence on nickel being electrodeposited causes the growth of length and thickness of the deposits at the direction of force action with a modification of their configuration depending on overload values.

Thus under minor overload ($k = 35$) the discussed change of form is seen as thickening of the edge of a

nickel deposit (Fig. 8 b). Such spherical segment bulge is more clear-cut than similar one of a copper deposit (Fig. 6 b). Seemingly it can be explained by finer crystal structure of nickel being electrodeposited in comparison with copper structure.
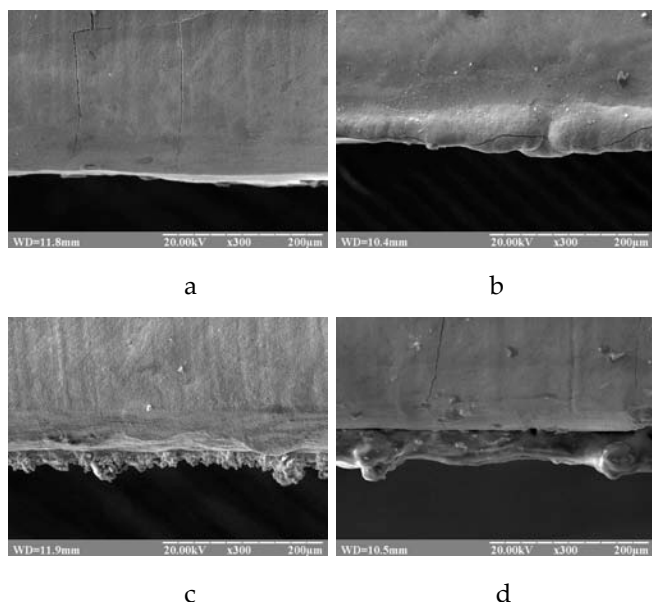


a           b

c           d

FIG. 8 SCANNING ELECTRON MICROSCOPY IMAGES OF THE FAR EDGE OF NICKEL DEPOSITS DEMONSTRATING A CHANGE OF THEIR FORM DURING ELECTRODEPOSITION UNDER THE INFLUENCE OF A CENTRIFUGAL FORCE PROPORTIONAL TO ACCELERATION OF $1G$ (A) – INITIAL CONDITION, $35G$ (B), $314G$ (C) AND $872G$ (D) THE FORCE IS DIRECTED FROM TOP TO BOTTOM

The further change of form of a deposit of nickel being electrodeposited with the increase of overload is seen as gradual growth of its length in the direction of the action of a centrifugal force (Fig. 8 c). Fig. 8 d illustrates new form of a nickel deposit obtained as a result of significant force influence ($k = 872$) parallel to its crystallization front during electrodeposition. There is a layer of solidified liquid phase of nickel 40-50 m thick beyond the copper cathode along its edge. Multi-layer formations in the direction of the action of the force, smooth relief and globular bulges of this grown layer prove the fact of its formation by solidification of metallic liquid wave-like layers.

As a result of solidification of metallic liquid phase, the areas of a nickel deposits going beyond the edge of the cathode in the direction of the force influence can be considered (Fig. 9). It should be mentioned that morphologies of the areas of deposits of metals (nickel and copper) being electrodeposited under minor force influence differ insignificantly (Fig. 9 a and Fig. 7 a). With the increase of overload, the differences of morphologies of the areas of nickel and copper

become more essential, but the general tendency of differentiation of structure of the areas going beyond the edge of the cathode remains (Fig. 9 b and Fig. 7 b).
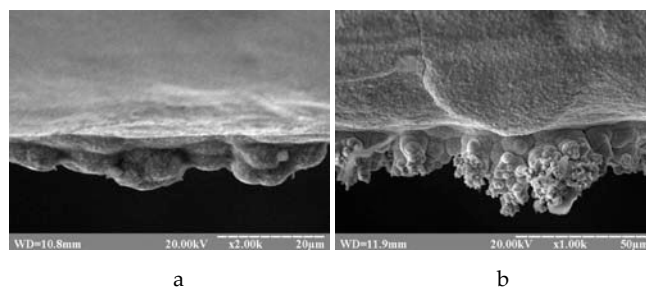


a           b

FIG. 9 SCANNING ELECTRON MICROSCOPY IMAGES OF THE FAR EDGE OF NICKEL DEPOSITS SHOWING MORPHOLOGY OF THE AREAS GOING BEYOND THE EDGE OF THE CATHODE DEPOSITS WERE OBTAINED BY ELECTRODEPOSITION UNDER FORCE INFLUENCE PROPORTIONAL TO ACCELERATION OF $140G$ (A) AND $314G$ (B). THE FORCE IS DIRECTED FROM TOP TO BOTTOM

A feature of configuration of nickel deposits under force influence parallel to their crystallization front is wave-like form of the far edge of the deposit at the direction of a centrifugal force action (Fig. 10 a). This form of the edge of the deposit is similar to wave-like form of the edge of copper deposit (Fig. 10 b). However, it is formed not as a result of growth of dendrite areas but due to the gathering of globular particles at the edge of the deposit. In Fig. 10 a, it is clearly seen that some globular particles are ingrown in nickel matrix which is an indication of its solidification from liquid state. This ingrowing effect intensifies at high overloads.
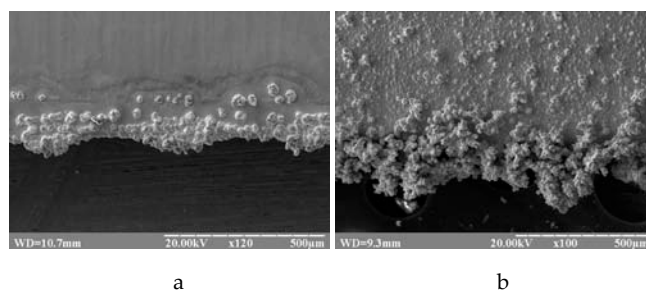


a           b

FIG. 10 SCANNING ELECTRON MICROSCOPY IMAGES OF THE FAR EDGE OF NICKEL (A) AND COPPER (B) DEPOSITS ILLUSTRATING FEATURES OF THEIR CONFIGURATION UNDER FORCE INFLUENCE PROPORTIONAL TO ACCELERATION OF $140G$ (A) AND $1256G$ (B) THE FORCE IS DIRECTED FROM TOP TO BOTTOM

It should be mentioned that with the increase of overload during metals electrodeposition, the quantity of glassy fragments of solidified foam ingrown in the edges of the areas beyond the cathode increases (Fig. 6, c-f; 7, b-d; 8, c, d; 9, b and 10, b). Nickel deposits in contrast to copper ones contain such inclusions not

only in the edges but also on the surface of the areas near the edges. For example the glassy inclusions partially ingrown in nickel matrix are shown at Fig. 11.
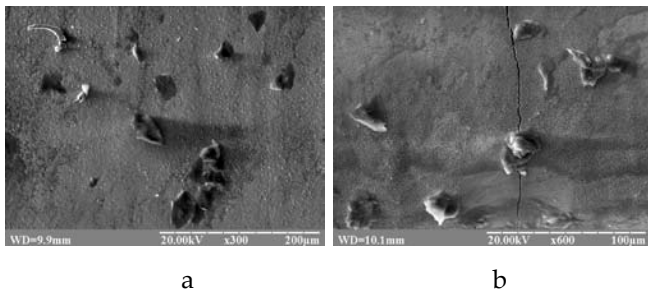


a                                    b

FIG. 11 SCANNING ELECTRON MICROSCOPY IMAGES OF GLASSY INCLUSIONS ON THE SURFACE OF NICKEL ELECTRODEPOSITS CENTRIFUGAL FORCE IS PROPORTIONAL TO ACCELERATION OF 314$G$ (A) AND 872$G$ (D) AND DIRECTED FROM TOP TO BOTTOM.

Thus, a change of form of metals electrodeposits during their electrochemical deposition under force influence parallel to the crystallization front proves that metallic materials being electrodeposited pass through a stage of liquid state.

### Idea Four and Its Realization

Assume that a metallic material during electrochemical deposition really passes through a stage of liquid state, then under the influence of a centrifugal force parallel to the crystallization front on the clusters of atoms, which have not yet formed a three-dimensional lattice typical for crystal state, it should be expected their movement at some distance at the direction of the force action. As a result of such movement, the combination of the clusters of atoms into larger formations (so called micro-droplets) will be easier. Such micro-droplets will form layers of liquid phase continuously replenishing during electrodeposition. At the increase of mass and size of liquid layers their shift in the direction of action of a centrifugal force will increase.

If the discussed phenomenon is valid, then at significant value of a centrifugal force acting parallel to the crystallization front it should be expected the movement of liquid layers toward the edge of the cathode and then beyond the edge of the cathode and next beyond the edge of previous solidified layers of metals being electrodeposited. This will cause predominant development of a deposit of a metal being electrodeposited beyond the edge of the cathode in the direction of the force action.

For the investigation of features of formation of the deposits of copper and nickel their cross-sections

along the direction of a centrifugal force action were prepared. The deposits, obtained in the centrifuge under similar conditions but when the rotor was at rest (i.e. at $k = 1$), were used as reference samples.

As a result of completed investigations, the effect of predominant development of deposits of metals being electrodeposited beyond the edge of the cathode at the direction of the force action parallel to the crystallization front was found. Thus, in Fig. 12 a, it is seen that the edge of copper deposit, obtained under usual conditions on thin nickel cathode has almost the same thickness on all its areas. At that the edge of copper deposit peeled off the end of the cathode due to low adhesion (peeling spot is shown by an arrow).
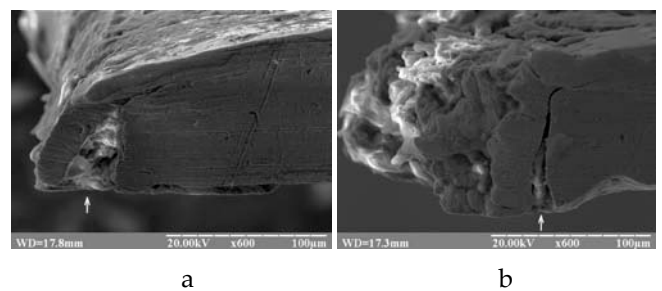


a                                    b

FIG. 12 SCANNING ELECTRON MICROSCOPY IMAGES OF THE CROSS-SECTION OF THE FAR EDGE OF COPPER DEPOSITS ALONG THE ACTION OF A CENTRIFUGAL FORCE PROPORTIONAL TO ACCELERATION OF 1$G$ (A) – INITIAL CONDITION AND 872$G$ (B), DEMONSTRATING THE EFFECT OF DEVELOPMENT OF THE DEPOSITS OF METALS BEING ELECTRODEPOSITED BEYOND THE EDGE OF THE CATHODE UNDER THE FORCE INFLUENCE THE FORCE IS DIRECTED FROM THE RIGHT TO THE LEFT

The image of cross-section of the edge of copper deposit formed under the influence of a centrifugal force of a significant value (Fig. 12 b) also indicates peeling off the edge of the deposit at the end of the cathode (peeling spot is shown by an arrow). But a form of the edge of this deposit is significantly different from the edge of usual deposit. The difference is the growth of its length by more than 100 µm along the force action (Fig. 12 b). Such result indicates that copper deposit during its electrodeposition was developing under the influence of a centrifugal force beyond the edge of the cathode.

If to compare thickness of the deposits electrodeposited in the field of a centrifugal force at various distances from the far edge of the cathode, significant thickening of the deposits in the direction of the force action is obvious. Thus under usual conditions of electrodeposition thickness of copper deposit at various distances from the far edge of the cathode is almost the same and equal to 10 µm (line 1 at Fig. 13).
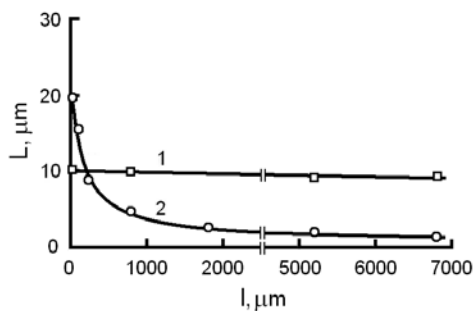
115

FIG. 13 CHANGE OF THICKNESS OF ELECTRODEPOSITED COPPER DEPOSITS (*L*) WITH AN INCREASE OF THE DISTANCE FROM THE FAR EDGE OF THE CATHODE (*L*) DEPOSITS WERE OBTAINED UNDER THE ACTION OF A CENTRIFUGAL FORCE PROPORTIONAL TO ACCELERATION OF 1*G* (1) – INITIAL CONDITION AND 1256*G* (2)

Under the action of a centrifugal force the deposits being electrodeposited thicken significantly toward the edge of the cathode at the direction of the force action (curve 2 at Fig. 13). Thus at the distance of $6800 \sim 1840$ μm from far edge the thickness of the deposit obtained at overload of $k = 1256$ is just $1.58 \sim 2.55$ μm, and with a decrease of *l* values to 800 and 230 μm the deposit thickens up to 4.88 and 9.09 μm respectively. And at the minimum distance from the far edge of the cathode (20 μm) the value of thickness of this deposit is two times as large as respective value of the deposit obtained under usual conditions (Fig. 13).

Such significant thickening of the deposits at the direction of the action of a centrifugal force can be explained by the combination of the clusters of atoms, which are in liquid state, in micro-droplets forming layers which move a metal being electrodeposited toward the edge of the cathode in a wave-like manner. Thus as an example in Fig. 14, metallic waves formed on the surface of the deposit of copper being electrodeposited at overload of $k = 1256$ are shown.



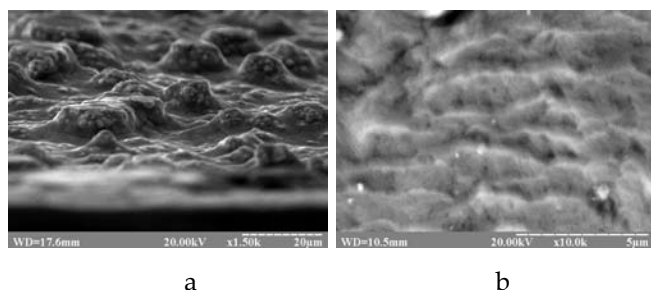a                                                b

FIG. 14 SOLIDIFIED WAVES OF LIQUID PHASE OF COPPER DEPOSIT BEING ELECTRODEPOSITED UNDER THE INFLUENCE OF A CENTRIFUGAL FORCE ACTING PARALLEL TO THE CRYSTALLIZATION FRONT WITH ACCELERATION PROPORTIONAL TO 1256*G*: A – SIDE VIEW (THE FORCE IS DIRECTED FROM THE RIGHT TO THE LEFT), B – TOP VIEW (THE FORCE IS DIRECTED FROM TOP TO BOTTOM)

It should be mentioned that wave-like flow of surface layers of metals being electrodeposited is the main motion of their liquid phase under the influence of a centrifugal force. Though, besides wave-like flow of layers of metals being electrodeposited (Fig. 15 a) overflow of layers (Fig. 15 b), their foaming (Fig. 15 c) and ripples on their surface (Fig. 15 d) occur depending on values of overload.

At Fig. 15 globular solid particles of copper deposit, moving under the influence of a centrifugal force toward the edge of the cathode, are seen. With an increase of overload the size of particles, moved relative to the deposit surface, increases significantly. Ingrowth of particles in the matrix (Fig. 15 a, b) and configuration of the vacant places, that were previously occupied by such particles (Fig. 15 b), indicates solidification of copper matrix from liquid state.

Similar results were also obtained during investigations of development features of nickel deposits being electrodeposited beyond the edge of the cathode in the direction of the force influence. Therefore, predominant development of deposits of metals being electrodeposited beyond the edge of the cathode in the direction of the action of a centrifugal force parallel to the crystallization front is a sufficient confirmation of the validity of the discussed phenomenon.

Thus, the obtained results prove the validity of the phenomenon of phase formation through a stage of liquid state in metallic materials being electrodeposited.

## Conclusions

The found effect of increase of density of metals being electrodeposited under the influence of a centrifugal force directed perpendicular to the crystallization front confirms the validity of the phenomenon of phase formation through a stage of liquid state in metallic materials being electrodeposited. Wave-like flow of surface layers of metals being electrodeposited under the influence of a centrifugal force acting parallel to the crystallization front as well as bending of waves by mechanical hindrances and formation of foam on the crests of waves prove the validity of this phenomenon. Change of form of the deposits of metals being electrodeposited under the influence of a centrifugal force including the growth of length and thickness of the deposits at the direction of force action with a modification of their configuration depending on

overload values prove the validity of the discovered phenomenon. Predominant development of deposits of metals being electrodeposited beyond the edge of the cathode in the direction of the action of a centrifugal force parallel to the crystallization front confirms the validity of the discussed phenomenon.



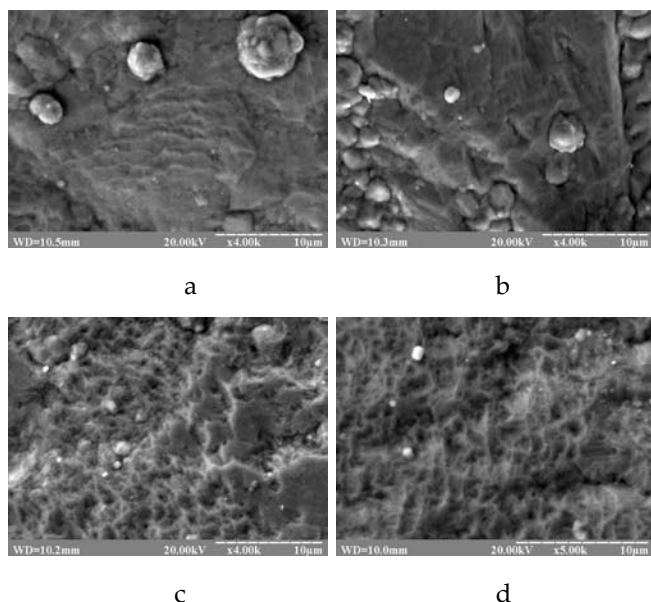a                  b

c                  d

FIG. 15 SCANNING ELECTRON MICROSCOPY IMAGES OF THE SURFACE OF COPPER DEPOSITS BEING ELECTRODEPOSITED UNDER THE INFLUENCE OF A CENTRIFUGAL FORCE, ILLUSTRATING MORPHOLOGY OF SOLIDIFIED LIQUID PHASE DEPENDING ON OVERLOAD VALUE: A AND B – OVERLOAD IS 1256, C AND D – 558 THE FORCE IS DIRECTED FROM TOP TO BOTTOM

## References

[1] O. B. Girin and G. M. Vorob'ev, "Regular Change of Substructure of Electrodeposited Metals with the Increase of the Nuclear Charge of their Atoms", *Zhurnal Vsesoyuznogo Khimicheskogo Obshchestva imeni D.I. Mendeleeva*, 1986, vol. 31, pp. 592–594 (In Russian).

[2] O. B. Girin and G. M. Vorob'ev, "Change of Diffraction of X-Rays Dissipated by Metals during their Electrolytic Deposition", *Zhurnal Fizicheskoi Khimii*, 1988, vol. 62, pp. 1347–1349 (In Russian).

[3] O. B. Girin, "Phenomenon of Precipitation of Metal Being Electrodeposited, Occurring via Formation of an Undercooled Liquid Metal Phase and its Subsequent Solidification. Part 1. Experimental Detection and Theoretical Grounding", *Materials Development and Processing*, 2000, vol. 8, pp. 183–188.

[4] O. B. Girin, "Phenomenon of Precipitation of Metal Being Electrodeposited, Occurring via Formation of an Undercooled Liquid Metal Phase and its Subsequent Solidification. Part 2. Experimental Verification", *Materials Development and Processing*, 2000, vol. 8, pp. 189–194.

[5] O. B. Girin, "Phenomenon of Structure Formation of Metals being Electrodeposited via a Supercooled Metal Liquid, and its Use for the Development of Advanced Technologies of Depositing New Types of Protective Composite Coats on Canned Food Steel Sheet", in *Proc. AFES'2004*, Paris, 2004, pp. 142–147.

[6] O. B. Girin, "Structure Formation of Metals being Electrodeposited through a Metal Liquid as a Tool for Surface Quality Upgrading of Canned Food Steel Sheet", in *Proc. AFES'2005*, Hong Kong, 2005, pp. 101–103.

[7] O. B. Girin, "Phase Transformations in the Metallic Materials being Electrodeposited", in *Proc. AFES'2006*, Davos, 2006, pp. 76–81.

[8] O. B. Girin, "Phase Transformations in the Metallic Materials being Electrodeposited and Their Application for the Development of Advanced Technologies for Anticorrosive Protection of Canned-Food Steel Sheet", *Materials Science Forum*, 2007, vol. 561-565, pp. 2369–2372.

[9] O. B. Girin, "Phase and Structure Formation of Metallic Materials Electrodeposited via a Liquid State Stage: New Experimental Proof", *Defect and Diffusion Forum*, 2010, vol. 303-304, pp. 99–105.

[10] O. B. Girin and I. D. Zakharov, "Increase of Density of Metals being Electrodeposited Under the Influence of a Centrifugal Force", *Vostochno-Evropeiskii zhurnal peredovykh tekhnologii*, 2011, № 5/5, pp. 4–7 (In Russian).

**Oleg B. Girin** was born in Dnipropetrovsk region, Ukraine in 1952. In 1974 he graduated with honors from technological faculty of Dnipropetrovsk Metallurgical Institute and started his post-graduate course. In 1977 he completed the post-graduate course, and in 1990 ahead of the schedule – his doctorate course at this institution defending his doctorate's dissertation by specialty of "Physical Metallurgy and Heat Treatment of Metals". He has PhD (1981) and DSc (1991) degrees, certificates of Senior Research Fellow (1992) and Professor (2002).

During 1977-1998 he worked at Dnipropetrovsk Metallurgical Institute as junior (1977-1981), senior (1981-1991) and leading research fellow (1991-1998). Since 1998 he has been working at Ukrainian State University of Chemical Technology as the HEAD OF THE MATERIALS SCIENCE DEPARTMENT, that was established with his direct involvement, and since 2010 – as the VICE-RECTOR OF SCIENCE. Main directions of his scientific activity are the investigation of laws of structure formation of metallic materials and the development of advanced technologies for obtaining of coatings with enhanced properties. Under his scientific supervision the advanced technologies for producing new types of protective coatings on metal-roll were developed and the special-property composite film materials were created. He obtained priority results in investigations of influence of nanocrystal, amorphous and oriented structure on the properties of electrochemical coatings.

Prof. Girin has won a worldwide recognition as a scientist. Under scientific supervision of Prof. Girin and with his involvement three international competitions of R&D projects financed by the governments of the USA, Canada and the European Union have been won. He has been elected as an active member of the New-York Academy of Sciences (1997), TMS (1995), ASM (2004) and ECS (2005). For the outstanding contribution to electrochemical materials science and unique developments in the field of special materials science Prof. Girin was awarded with The International Einstein Award for Scientific Achievement (United Kingdom, 2011), the Order Badge "K.K. Rokossovsky" (Russian Federation, 2011), the medal "Great Minds of the 21st Century" (USA, 2011), the medal "2000 Outstanding Intellectuals of the 21st Century" (United Kingdom, 2010), the certificate "Decree of Merit" (United Kingdom, 2010), the Certificate of Honors of the Cabinet of Ministers of Ukraine (2005), the Badge of Honors "For Scientific Achievements" (Ukraine, 2005).

# Hybrid Metal Foams

Mechanical Testing and Determination of Mass Flow Limitations During Electroplating

Anne Jung [*1], Michael R. Koblischka[2], Erhardt Lach[4], Stefan Diebels[1], Harald Natter[3]

[1]Department of Applied Mechanics, Saarland University, 66123 Saarbruecken, Germany

[2]Department of Experimental Physics, Saarland University, 66123 Saarbruecken, Germany

[3]Department of Physical Chemistry, Saarland University, 66123 Saarbruecken, Germany

[4]French German Research Institute of Saint-Louis, 68300 Saint-Louis, France

[*1]anne.jung@mx.uni-saarland.de;

*Abstract*

Electrodeposition is a non-line of sight deposition technique which is also applicable for complex 3D structures. Even with this outstanding coating method there is a challenge in electroplating of complex 3D materials with a high porosity. In this work we developed special process parameter regarding the design of the plating cell and deposition parameter to ensure a nearly homogeneous coating of open cell metal foams. Based on field scans of the magnetic flux density a technique for the determination of the coating thickness distribution of magnetic coatings in a foam has been developed. The deposition process and thus the coating thickness distribution of porous 3D cathodes strongly depends on mass transport limitations. Two qualitative models to describe the mass transport limitations for direct current plating and pulsed electrodeposition can be deduced of the field scans of the magnetic flux density. X-ray computed tomography shows hydrogen evolution as a further coating-problem. Quasi-static compressions tests have been performed on nickel and copper coated foams, respectively. The coating metal has a significant effect on the mechanical properties of such a hybrid foam consisting of a coating on an aluminium substrate foam.

*Keywords*

*Electrodeposition; Metal Foams; Nanocrystalline; Magnetic Flux Density; Compression Tests*

## Introduction

Metal foams are a very interesting class of biomimetric structures. They are highly porous cellular metals with a 3D open network of pores and mimic the construction elements of bones, wood or cork [1]-[2]. According to this spectacular mesoscopic structure, this structuring shows a high stiffness-to-weight ratio and an excellent energy absorption capacity. Open cell metal foams especially based on aluminium became of significant interest for applications in aerospace, automotive and mechanical engineering [3]-[4]. For these fields of application they are used as lightweight construction elements, energy absorber or for structural damping. Further applications are filters, heat exchangers and catalyst supports [3]-[5].

Based on the open porous structure of metal foams, they can be used as cathode in electroplating processes for reinforcement of lightweight aluminium foams. Only a few works [6]-[7] are known about this topic. These works describe the coating of very thin foams with a thickness of less than 12 mm. The general problem is the ratio of the coating thickness of the outer struts and the centre is about 2 which means, there is a highly inhomogeneity of the coating thickness distribution over the foam cross section. As shown by Euler [8] the deposition process and hence the thickness of the coating in porous electrodes are strongly influenced by mass transport limitation. A deeper understanding of this mass transport limitation is necessary to improve the homogeneity of the coating thickness distribution. Coating of metal foams can improve the mechanical properties or provide additional functions like corrosion resistance or catalytic activities. The excellent mechanical properties (stiffness and energy absorption) of a hybrid foam based on an aluminium foam with a nanocrystalline nickel coating have been shown in a previous work [9]. In this work we developed a qualitative model to describe the degree of inhomogeneity of the coating thickness distribution by measuring the magnetic flux density distribution of nickel coated foams. With these results it was possible to improve the coating process and to adopt to other coating metals like copper.

## Materials and Methods

*Plating Procedure*

Electrodeposition is a versatile and common non-line

of sight technique for the preparation of metals and alloys [10]-[12]. In his study aluminum foams (AlSi7Mg0.3 by m-pore, Dresden, Germany) with pore size of 10 ppi (pores per inch), were plated by direct current (DC) or pulsed electrodeposition (PED) with nanocrystalline nickel.

Before the electrodeposition an 8 steps pre-treatment (pickling and electroless deposition) is necessary to protect the aluminum based foams from dissolution in the acid electrolyte. The pickling does although improve the adhesion of the coating. The pretreatment process is outlined in Fig. 1.
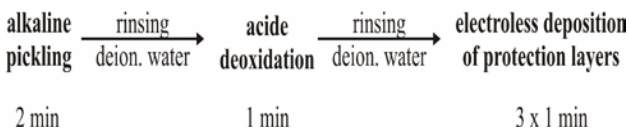


FIG. 1 PRE-TREATMENT OF THE ALUMINUM FOAMS

All steps were carried out at room temperature with rinsing in deion. water after each step. A commercial nickel sulfamate electrolyte with 110 g/L nickel (Enthone, GmbH, Langenfeld, Germany) was used at 50°C and a pH of 3.8. For the copper coating a copper sulfate electrolyte has been used (200 g/L $CuSO_4 \cdot 4H_2O$, 50 g/L $H_2SO_4$, 0.2 g/L surfactant, 40°C, pH = 1). The exact plating parameters are mentioned for each experiment.

In contrast to planar electrodes the plating of 3D porous materials requires a special anode-cathode configuration. The anode consists of a double-walled hollow cube, built of expanded titanium metal and filled with nickel pieces (Ni, A.M.P.E.R.E. GmbH, Dietzenbach, Germany) or even copper tubes as sacrificial anode. The cathode consists of an aluminum foam, placed in the centre of the cage-like anode. The depositions were carried out in a thermostated electrolysis cell with a volume of 3500 ml.

*Mass Transport Limitation*

Coating of such complex three dimensional electrodes causes a special mass transport limitation. In the case of DC-plating there are two concentration zones in front of a planar bulk electrode. The first zone is the bulk electrolyte; with a constant concentration of the metal ions. In the second zone between the cathode and the bulk electrolyte consists of a linear metal ion gradient. At the limiting diffusion current the concentration at the cathode surface is zero [13]. Open-cell metal foams are substantially more complex three-dimensional electrodes. The above mentioned

concentration profile for planar electrodes has to be expanded into a third dimension. During the electrodeposition of foams each of the struts can act as a planar electrode as described above. The problem is outlined in Fig. 2. It describes an open cell metal foam plunged into an electrolyte. If no current is applied, the metal ions are homogeneously distributed over the cross-section of the foam. After applying a current, all metal ions within and in the vicinity of the foam will be spontaneously deposited. To continue the coating process, metal ions have to diffuse from the bulk of the electrolyte to the centre of the foam.

Based on the fact, that there is a deposition of metal ions all way from the outer regions of the metal foam to the centre of the foam, only a few ions will reach the centre of the foam. In the inner of the foam occurs an ion diffusion due to a gradient in the ion concentration. This mass transport limitation by diffusion during the plating process causes a non-uniform coating thickness distribution on the struts. A second effect which let to a certain inhomogeneity of the coating is the electromagnetic shielding from outer ligaments of the foam which acts as a faraday cage [6].
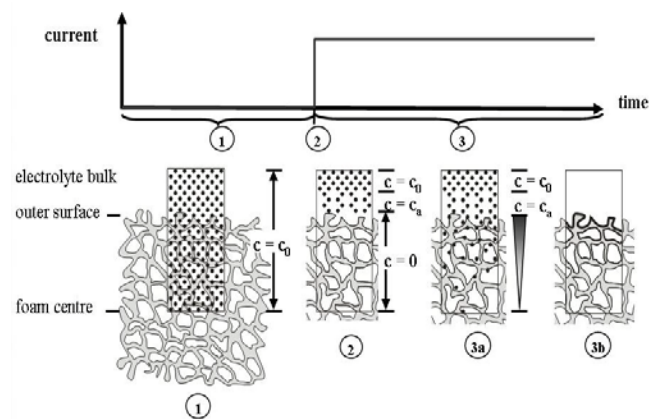


FIG. 2 SCHEME OF THE METAL IONS DISTRIBUTION IN THE FOAM DURING DIRECT CURRENT PLATING (DC). (1) ZERO CURRENT, (2) APPLIED CURRENT: DEPLETION OF METAL-IONS IN THE CENTRE OF THE FOAM (3A) DIFFUSION OF METAL IONS FROM THE BULK ELECTROLYTE INTO THE FOAM, (3B) INHOMOGENEOUS COATING THICKNESS DISTRIBUTION DUE TO MASS TRANSPORT LIMITATION

In contrast to planar electrodes the plating of 3D porous materials requires a special anode-cathode configuration. The anode consists of a double-walled hollow cube, built of expanded titanium.

Pulsed electrodeposition should produce a more homogeneous coating thickness distribution than DC plating. Fig. 3 shows a scheme of the distribution of metal ions in a foam during the pulsed
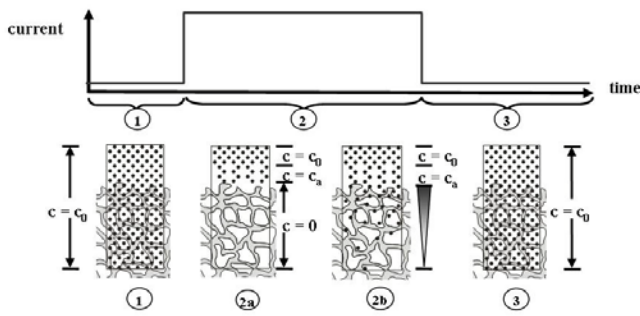
electrodeposition process.



FIG. 3 SCHEME OF THE METAL IONS DISTRIBUTION IN THE FOAM DURING PULSED ELECTRODEPOSITION (PED). (1) ZERO CURRENT ($T_{OFF}$-TIME) (2) CURRENT PULSE ($T_{ON}$-TIME), (2A) DEPLETION OF THE METAL-IONS IN THE FOAM, (2B) DIFFUSION OF METAL IONS FROM THE ELECTROLYTE BULK INTO THE FOAM CENTRE AND DEPOSITION, (3) $T_{OFF}$ TIME: THE METAL IONS ARE ABLE TO DIFFUSE TO THE FOAM CENTRE WITHOUT DEPOSITION

Similar to the direct current plating process, the metal ions in the vicinity of the foam surface will be spontaneously deposited during the $t_{on}$-time. There is the depletion of the electrolyte in the pores. In the following $t_{off}$-time the metal ions diffuse from the electrolyte bulk to the foam centre without deposition at the outer ligaments of the foam. Increasing $t_{off}$-times should improve the homogeneity of the coating thickness distribution.

## Characterization

### Scanning of the Magnetic Flux Density

A method to visualize the coating thickness distribution of a coated foam sample is a prerequisite for the enhancement of the homogeneity of the coating thickness by optimizing the plating parameters. For ferromagnetic coatings like nickel, we developed a method to visualize the metal distribution by scanning of the magnetic flux density distribution in analogy to the trapped field scans performed now routinely on bulk high-Tc superconductors [14]-[16]; Christides et al. were also applying this technique to bulk permanent magnets [17]. The coated aluminum foam cubes are cut into several rectangular plates. The plates are introduced into a Helmholtz coil with a homogeneous magnetic field of 256 mT oriented perpendicular to the longest axis of the foam pieces to force a defined initial magnetic state on the foam plates. The metal distribution of each foam plate is determined by measuring the remnant magnetic flux density distribution Bz(x,y) by scanning the surface of the foam with a commercial Hall probe (Arepoc, Bratislava, Slovakia; magnetic resolution 0.1 G) in a

fixed distance of 1.5 mm above the sample surface. Fig. 4 shows the five measuring planes (MP) of a foam sample which was cut into four plates. The measuring setup for the field scan of nickel-coated metal foams is also displayed.
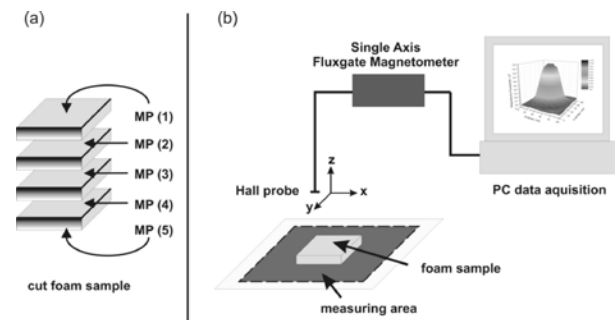


FIG. 4 (A) THE MEASURING PLANES OF A FOAM SAMPLE AND (B) SCHEMATIC DRAWING OF THE MEASURING SETUP

A Hall probe fixed on a x-y-z-stage is able to scan in a distance of 15 mm above the foam plates. The dimensions of the measuring area were the three-fold of the dimensions of the foam in x- and y-direction. The information about the thickness distribution and its spatial distribution results from the measured trapped field. Additional information about this method supplied for coated metal foams can be found in a previous work [18].

### Characterization of the Nanostructure

The crystallite size, crystallite size distribution and microstrain of the nanostructured metallic coatings have been determined by X-ray diffraction (XRD; Siemens D500, Bruker AXS, Germany) using a modified Warren-Averbach method [19]-[21]. The nickel coatings of all samples have a crystallite size of 43 nm ± 2 nm. A characterization of the morphology of the foam substrates and coatings has been carried out using scanning electron microscopy (SEM; Jeol JSM 7000 F). To have a closer look on the homogeneity and quality of the coating thickness over the foam and the structure of the foam, X-ray computed tomography (Fraunhofer IZFP, Saarbrücken, Germany) has been performed on coated and uncoated aluminum foams.

### SEM and X-ray Computed Tomography

The surface morphologies of the uncoated aluminum foams and a nickel coating are shown in Fig. 5. The uncoated aluminum foams have a rough surface built of bumps. The nickel coating has a smoother surface morphology. Round bumps which are close to each other built a fully covering coating. This cauliflower-like structuring results from a radial grain growth process resulting from a hemispherical ion diffusion.

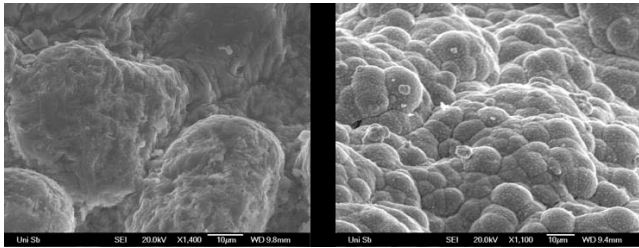This structure increases the specific surface area of a foam.



FIG. 5 SEM-IMAGES OF AN UNCOATED ALUMINUM FOAM (X1400, LEFT) AND THE DC NI COATING (X1100, RIGHT)

Fig. 6 shows X-ray computed tomograms of an uncoated aluminum foam and a nickel coated foam with a coating thickness of 150 μm (deposited at a DC current density of 1.1 mA/cm²). The tomogram outlines an almost homogeneous coating thickness distribution for the cross-section of the foam. Due to the side reaction of hydrogen evolution, the coating contains some pinhole defects caused by the sticking hydrogen. To avoid the embrittlement of the coating by grain refiners, we do not use any surfactants.
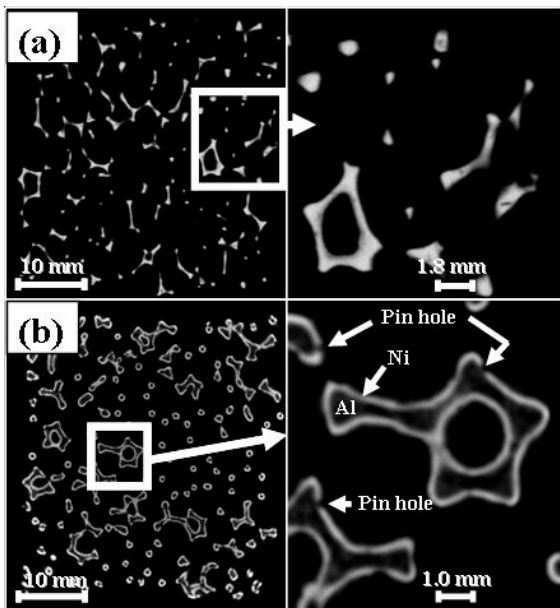


FIG. 6 X-RAY COMPUTED TOMOGRAMS OF AN UNCOATED ALUMINUM FOAM (A) AND A NICKEL COATED ALUMINUM FOAM WITH A COATING THICKNESS OF 150 μM

### Quasi-static Compression Tests

In order to investigate the effect of different coating metals and coating thicknesses, cubic 10 ppi aluminium foams with an edge length of 40 mm have been coated with nickel and copper, respectively. The theoretical coating thicknesses vary in 50 μm steps between 0 and 250 μm for each coating metal. The hybrid foams have been tested on an INSTRON universal testing machine under compressive loading at strain rates of about $5 \cdot 10^{-3}$ s⁻¹. According to the very complexe structure of the metal foams, there is a common significant scattering in the results. Based on this fact and for a better statistics, each sample type has been tested at least three times.

## Results and Discussion

### Field Scans of the Magnetic Flux Density

In order to optimize the applied average current density for DC nickel plating, cubic 10 ppi foams (40 x 40 x 40 mm³) were coated at different current densities. The theoretical all-over coating thickness should be 20 μm. After the plating process each foam was cut into rectangular plates with a thickness of 10 mm. Trapped field scans of the magnetic flux density, $B_z$, were performed on each of these foam cuts. Maximal relative flux densities results for four plates of foam samples coated at different applied current densities are shown in Fig. 7.
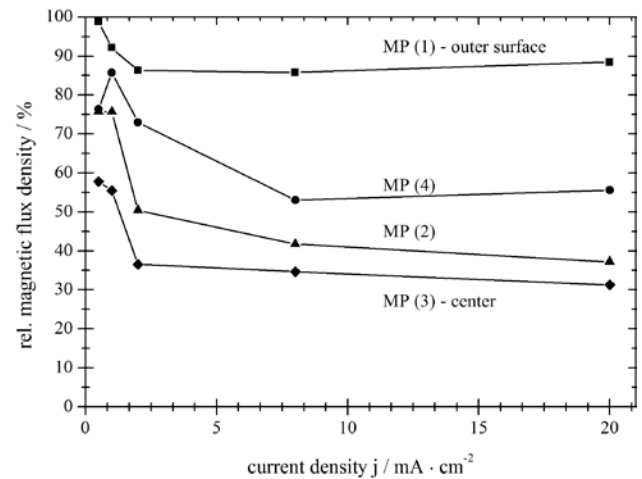


FIG 7 RELATIVE MAGNETIC FLUX DENSITIES OF FOAMS VS. APPLIED CURRENT DENSITY

The relative magnetic flux density has been determined from the field scans as the ratio of the maximal trapped magnetic flux density of each measuring plane and the maximal magnetic flux density of the complete foam which is normally the trapped flux density of the bottom of the foam (MP (5)).

The native foam morphology and structure of the pores is not exactly the same for different foam positions. As a result of this structural inhomogeneity and the statistical distribution of the pores and struts in the foam structure there is a difference in the magnetic flux density of MP (1) and MP (5) although

there should be the same coating thickness. For measuring planes of similar positions, the coating thickness should be the same. The difference in the relative magnetic flux density of the measuring planes (2) and (4) is an artifact of the penetration depth of the Hall probe and hence a consequence of the different measuring volumes (see grey color gradient in Fig. 4). The measuring volume of MP (2) is closer to the foam centre than for MP (4). As a result of the difference in the position of the measuring volumes MP (2) has a lower magnetic flux density than MP (4).

Foams coated with high average current densities show strong inhomogenities in the coating thickness distribution from the outer parts of the foam to the centre. For increasing current densities the relative magnetic flux density of each cut reaches a nearly constant level.

The curve shape of the magnetic flux density for a distinct cut can be explained by the concept of the limiting diffusion current (LDC) of metal ions during the electroplating and indicates a direct proportionality between the magnetic flux density and the LDC of the foam. Each cut has a distinct local LDC. There is a gradient of the metal ions in the electrolyte in the inner of the pores; hence the LDC decreases from regions close to the outer surface to the center of the foam. Based on this concept of local limiting diffusion currents the magnetic flux density is proportional to the coating thickness distribution.

According to these considerations, an increase of the LDC will result in an improvement of the homogeneity of the coating thickness distribution. The LDC can be increased by the use of a more concentrated electrolyte, higher electrolyte temperatures or by an increase of the electrolyte flow through the foam. In this study the LDC has been enhanced by pumping the electrolyte through the foam during the plating process. For a current density of 1 mA/cm² the relative magnetic flux density and the coating thickness, respectively could be increased from 55.5% to 61.3% (in the center of the foam). For a current density of 20 mA/cm² an increase of the magnetic flux density from 31.3% to 44.0% can be found.

The enhancement of the coating thickness homogeneity by an increase of the electrolyte flow intensity is larger than by the reduction of the average current density. This is an evidence that the coating of metal foams via electrodeposition is subjected to very strong mass transport limitations.

Fig. 8 shows the relative magnetic flux densities for different current densities as a function of the position in the foams. For an increase of the current density the curve shape of the magnetic flux density shows more and more an exponential decay.
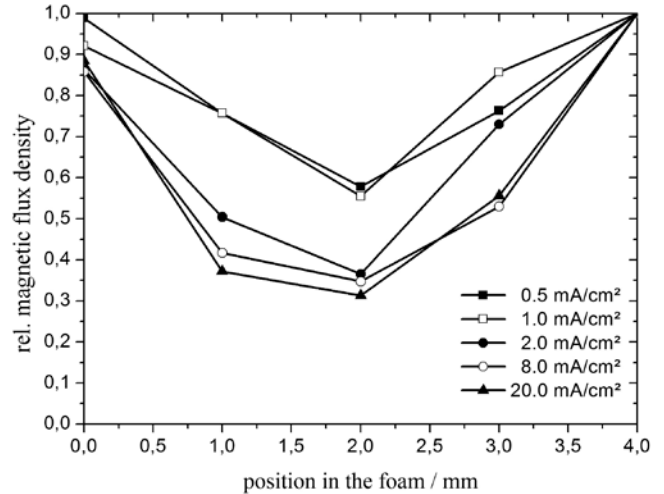


FIG. 8 RELATIVE MAGNETIC FLUX DENSITIES DETERMINED AT DIFFERENT FOAM POSITIONS. THE SAMPLES WERE PREPARED AT DIFFERENT CURRENT DENSITIES

### Mass Transport Limitation in Electrodeposition on Metal Foams

To get further information about the mass transport limitations, e.g. the metal ion concentrations during the electrodeposition, cubic 10 ppi foams (50 x 50 x 50 mm³) have been coated with nickel at an average current density of 8 mA/cm² by DC plating (experiment 1), DC with an increased electrolyte flow (pumping the electrolyte) through the foam (experiment 2) and by pulsed electrodeposition (PED) with a duty cycle of 30% and a frequency of 100 Hz (experiment 3). Up to the centre, the foams were cut into rectangular plates with a thickness of 5 mm. The resulting relative magnetic flux densities from the field scans as a function of the position in the coated foam are shown in Fig. 6. The magnetic flux density and hence the thickness of the nickel coating decreases from the outer surface to the center of the foam cube.

For the DC plated foam without pumping the electrolyte through the sample the gradient in the magnetic flux density between two cuts decreases linear to the center of the foam. The measurement ends in a kind of saturation point located near the center of the foam. Based on the direct proportionality between the magnetic flux density and the coating thickness there must be a proportionality to the current density at this position whereas the current

density is proportional to the slope of the ion concentration gradient in the foam. The curve shape of the magnetic flux density distribution for the DC plated foam is in good accordance to the current density distribution in thick porous electrodes made of manganese dioxide or other materials used for batteries [8], [22], [23].

The increase of the flow intensity of the electrolyte through the foam (experiment 2) increases the magnetic flux density of each cut in comparison to the DC plated foam of experiment 1 and hence increase the homogeneity of the coating thickness distribution. The gradient between the first three cuts of the foam of experiment 2 is lower than for the foam of experiment 1. The curve shape becomes more linear.
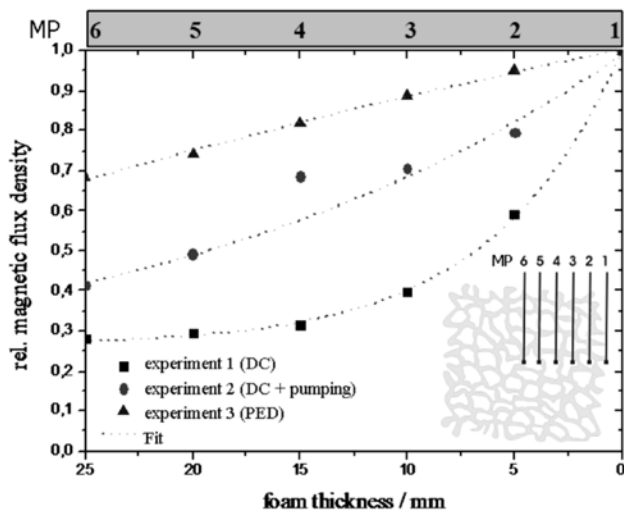


FIG. 9 RELATIVE MAGNETIC FLUX DENSITIES OF A FOAM COATED AT A CURRENT DENSITY OF 8 MA/CM² AS FUNCTION OF THE POSITION IN THE FOAM FOR DIFFERENT PLATING MODES

The foam coated by PED (duty cycle 30%, 100 Hz; experiment 3) has the most homogeneous coating thickness distribution. The coating thickness decreases linearly in direction to the foam center. The flux densities and hence the coating thicknesses for each measuring plane are much higher than for the two DC plated samples. The increase of the magnetic flux density in comparison to the DC plated samples is most distinct for the center of the foam (MP (6)).

Fig. 10 outlines the relative magnetic flux densities of foams coated at different current densities (duty cycle 50%) with and without enhanced hydrodynamics by pumping. As a fact of the lower degree of depletion of ions in the pores by PED higher coating thicknesses in the foam center can be achieved in comparison to DC plating. We find out that an increase of the

hydrodanamics is more important than a decrease of the applied current density. In recent publications concerning the coating of metal foams [6]-[7], an inhomogeneity factor of 2 (ratio of the coating thickness of the outer surface) was found. We could demonstrate that PED ($j_m$ = 2.4 mA/cm²) with the special anode-cathode configuration reduces this factor to 1.25 also for foams with a four-fold thickness. Lower current densities and lower duty cycles with an increased flow of the electrolyte through the foam would let to a further increase of the homogeneity of the coating thickness.
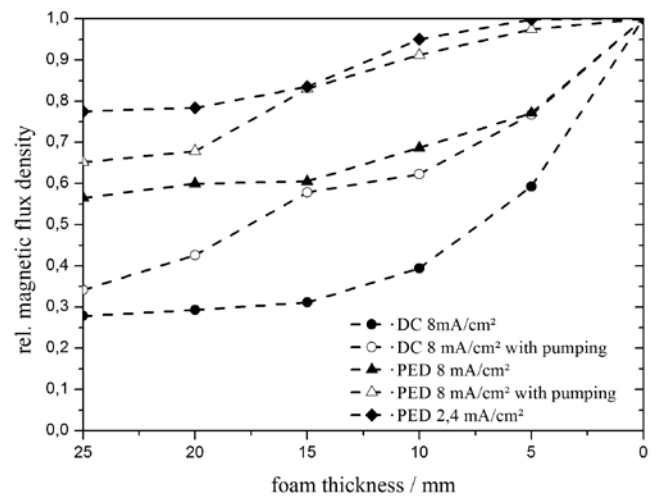


FIG. 10 RELATIVE MAGNETIC FLUX DENSITIES OF A FOAM COATED AT A CURRENT DENSITY OF 8 MA/CM² FOR DC AND PED (DUTY CYCLE 50%) AND PED AT A CURRENT DENSITY OF 2.4 MA/CM² FOR DIFFERENT HYDRODYNAMIC CONDITIONS

Based on these results (see Fig. 9 and 10) it is unavoidable to get a non-uniform coating thickness distribution from experiments without an increased electrolyte flow. In DC plating a very high electrolyte flow is necessary to improve the hydrodynamic conditions that almost uniform coating thickness distributions can be achieved. Also for PED it is not possible to deposit homogeneous coatings without a very strong electrolyte flow. Whereas lower pump intensities should be necessary for PED than for DC plating to implement the same degree of homogeneity. PED causes a more homogeneous coating thickness distribution but is does also changes the properties of the coating and hence the properties of the whole coating-foam composite by influencing the nanostructure. This change in the properties is not ever desirable. The crystallite size is more nanocrystalline and according to the grain boundary strengthening of Hall-Petch [24] the hardness and yield stress of a material are proportional to the reciprocal square root of the crystallite size. Coatings produced

by PED show a higher hardness and stiffness than coatings produced by DC plating. This hardness-increase is associated with a decrease of the coating ductility, hence the coating is more brittle.

A model to describe the mass transport limitation in direct current plating of metal foams on the basis of the above mentioned results is given in Fig. 11.
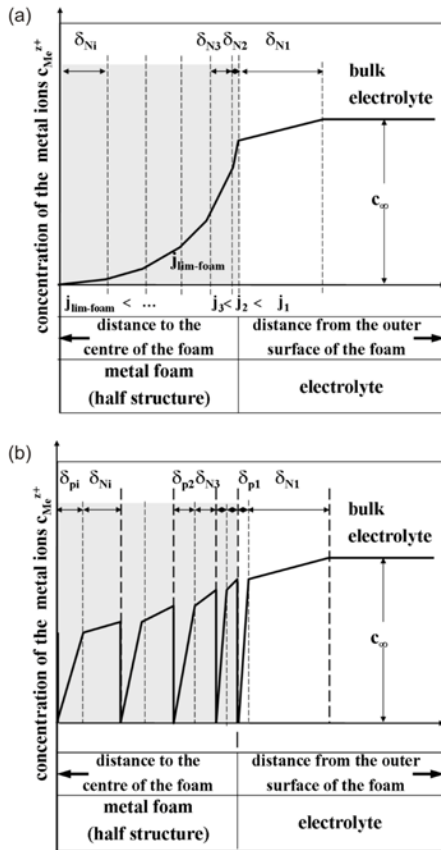


FIG. 11 MASS TRANSPORT LIMITATION MODEL FOR DIRECT CURRENT PLATING (A) AND PULSED ELECTRODEPOSITION (B) OF METAL FOAMS

The model is an extension of the two-dimensional mass transport limitation model for planar electrodes [13] in the third dimension into the foam structure and based on a superposition of Helmholtz layers $\delta_N$ with increasing layer thickness in direction to the foam centre. An increasing distance to the bulk electrolyte in direction to the foam center results to a gradual decrease of the concentration gradient between two neighboring Helmholtz layers.

At the outer surface of the foam the metal ions will be spontaneously deposited. This repeats at each Helmholtz layer $\delta_{Ni}$ in direction to the foam centre. Based on this large decrease in the ion concentration in the first pore layers the concentration gradient between two neighbouring Helmholtz layers (e.g. $\delta_{N2}$

$\rightarrow \delta_{N3}$) decreases up to the foam centre whereas the layer thickness increases. For each of these Helmholtz layer $\delta_{Ni}$ it exists a distinct local LDC $j_i$ which decreases from the first layer $\delta_{N1}$ to the last layer $\delta_{Ni}$ in the foam centre. The value of theses local LDCs ($j_i$) depends on the position in the foam. Foam increments can only be coated with nickel in the case that the applied current is less or equal to the local LDC. The LDC of the Helmholtz layer $\delta_{Ni}$ is the global limiting diffusion current of the foam $j_{lim-foam}$. For the same electrolyte the LDC of a theoretical planar electrode with the same side surface is much higher than the global LDC of foams. The local LDCs are in the range between the global LDC of the foam and the corresponding LDC of the theoretical planar electrode. Applying the LDC of a theoretical planar electrode on a foam, it will only be plated at the outer surface - the internal volume remains unplated.

This model is also valid for experiment 2, but the model has to be extended by terms of an increased diffusion or convection in the foam. This causes a reduction of the gradient between two neighboring Nernst layers and hence enlarges the layer thickness.

Due to the current alternation during the $t_{on}$- and $t_{off}$-times in PED the model has to be extended by a pulsating diffusion layer $\delta_{pi}$. The concentration of metal ions in this layer pulsates with the pulse frequency between the lowest concentration of the stationary diffusion layer and zero (directly in front of the electrode). The layer thickness of the pulsation diffusion layer decreases with an increasing pulse current density and $t_{on}$-time and thus with an increase of the duty cycle. Using the same average current density the thickness of the stationary diffusion layer, the Helmholtz layer, remains unchanged. For foams the second diffusion layer is immediately in front of each strut. In the model a pulsating diffusion layer has to be introduced between two Helmholtz layers. During the $t_{off}$-time there is the relaxation of the concentration of metal ions in the pulsating diffusion layer and thus the depletion of the electrolyte in direction to the center of the foam is diminished.

For direct current plating the shape of the concentration profile in Fig. 11 depends on the pore size, the foam thickness, the hydrodynamic conditions and the average current density. Furthermore in PED the curve shape depends on the duty cycle and the pulse frequency.

It is known that metal foams show an electromagnetic shielding effect [1], [4]. Based on this there could also be

a lowering of the applied current density in direction to the center of the foam by the foam framework itself according to the Faraday shielding effect. This shielding effect interferes with the above mentioned diffusion model. For this reason it is impossible to get a homogeneous coating thickness with a homogeneity factor of 1.0. m

### Optimization of the Coating Metal and Coating Thickness by Quasi-static Compression Tests

Fig.12 shows the stress-strain diagrams of nickel and copper based hybride foams, respectively. A coating with copper has no significant positive effect on the mechanical properties, whereas for the nickel coating, there is a linear increase of the plastic collapse stress and the plateau stress but a decrease of the compression and densification point with increasing coating thickness.
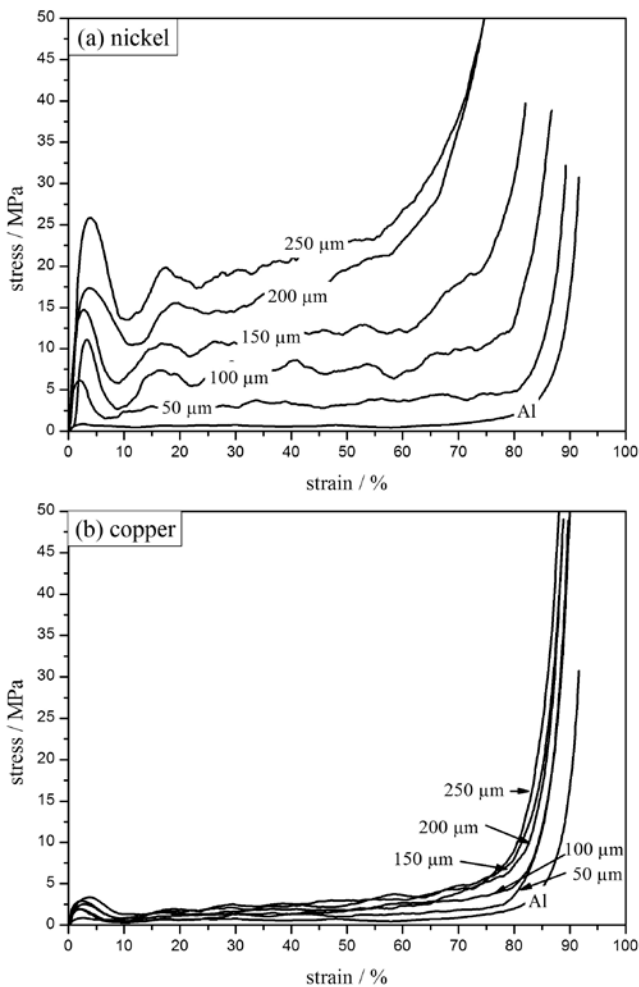


FIG. 12 STRESS-STRAIN DIAGRAMS OF NICKEL (A) AND COPPER (B) HYBRID FOAMS

The energy absorption capacity per foam thickness and per density of both types of hybrid foams is shown in Fig. 13 as function of the coating thickness.

The energy absorption capacity per thickness of the copper hybrid foams shows only a little increase in comparison to the uncoated aluminium foams but due to the larger coating thickness, the increasing mass overcompensates the positive effect of the coating. Hence, there is a halving of the specific energy absorption capacity per density for the hybrid foams in comparison to the aluminium foams. The reason for this behavior is on the one hand the worse mechanical properties of copper in comparison to nickel but principally on the other hand a bad adhesion of the copper coating on the aluminium foam due to corrosion effects during the coating process.
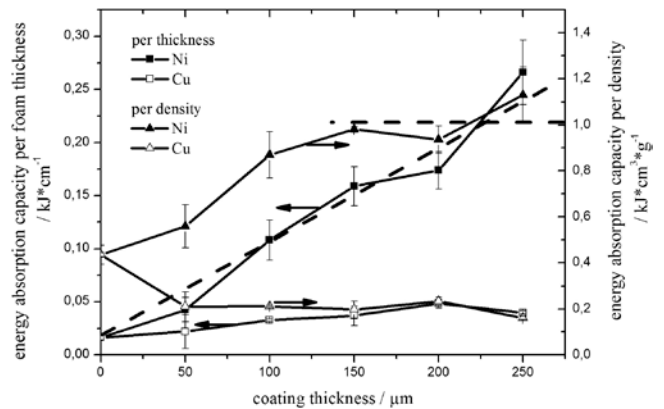


FIG. 13 DEPENDENCY OF THE SPECIFIC ENERGY ABSORPTION CAPACITY OF NICKEL AND COPPER BASED HYBRID FOAMS AS FUNCTION OF THE COATING THICKNESS

For the nickel hybrid foam there is not only a linear increase of the plastic collapse stress and the plateau stress but also of the energy absorption capacity per thickness. Even per density, nickel coated foams improve the energy absorption capacity. First, there is a linear increase with increasing coating thickness. At a coating thickness of about 150 μm nickel the increasing mass compensates the positive effect of the coating. This means, the optimal coating thickness for nickel hybrid foams is 150 μm. For this optimal coating thickness, there is an enhancement of the energy absorption capacity in comparison to the pure aluminium foams by a factor of about 10.

The exact enhancement effects are shown in Table 1.

For a better comparison of the performance of the nickel hybrid foams with the pure aluminium foams the theoretical plastic collapse stress and energy absorption capacity of pure aluminium foams with the same density as the hybrid foams have been calculated according to the model of Gibson and Ashby [25] and

Boonyongmaneerat et al. [7], respectively:

$$\sigma_{pcs} = \sigma_s C \left( \frac{\rho}{\rho_s} \right)^{3/2} \qquad (1)$$

$$U = \sigma_{pl} \left( \varepsilon_d - 0.5\varepsilon_{pl} \right) \qquad (2)$$

Whereas $\sigma_{pl}$ is the plastic collapse stress of the foam, $\sigma_s$ is the tensil strength of the aluminium matrix, $\rho$ is the density of foam, $\rho_s$ is the density of the aluminium struts and C is a material constant. U is the energy absorption capacity of the foam, $\sigma_{pl}$ the plateau stress, $\varepsilon_d$ the densification strain and $\varepsilon_{pl}$ the flow strain.

TABLE I COMPARISON OF THE MECHANICAL PROPERTIES OF ALUMINIUM FOAMS AND NICKEL HYBRIDE FOAMS WITH THE OPTIMAL COATING THICKNESS. THERE IS A DOUBLING OF THE SPECIFIC ENERGY ABSORPTION CAPACITY PER DENSITY

| property | Al foam | nickel hybrid foam 150 μm Ni | enhancement factor |
|---|---|---|---|
| Young's modulus [GPa·kg$^{-1}$] | 6.81 | 23.74 | 3.5 |
| plastic collapse stress [MPa·kg$^{-1}$] | 77.13 | 364.85 | 4.7 |
| plateau stress [MPa·kg$^{-1}$] | 65.75 | 252.38 | 3.8 |
| energy absorption capacity | | | |
| per foam thickness [kJ·cm$^{-1}$] | 1.65·10$^{-2}$ | 15.84·10$^{-2}$ | 9.6 |
| per density [kJ·cm$^3$·g$^{-1}$] | 0.415 | 0.978 | 2.2 |

Both, the theoretical aluminium foams and the nickel hybrid foams show a disproportional dependency of the plastic collapse stress with increasing density (cf. Fig. 14). According to Thornton [26], this is the proof that bending stresses play an important part during the collapse of the foam structure.

The hybrid foams gain advantage over the theoretical aluminium foams with the same density. This effect results from the increasing bending stiffness of the struts of the foam due to the hard nickel coating. The coating strengthens the outer fiber of the struts where the maximal stress during bending and buckling processes is localized. Depending on the coating thickness the aluminium strut has no portion on the outer fiber and this span completely over the thickness of the nickel coating. Hence, the strength of the strut is mainly governed by the nanocrystalline coating. An increasing coating thickness increases the cross section

of the struts and hence the moment of inertia. The enhancement of the bending stiffness arises from the enhancement of the moment of inertia.
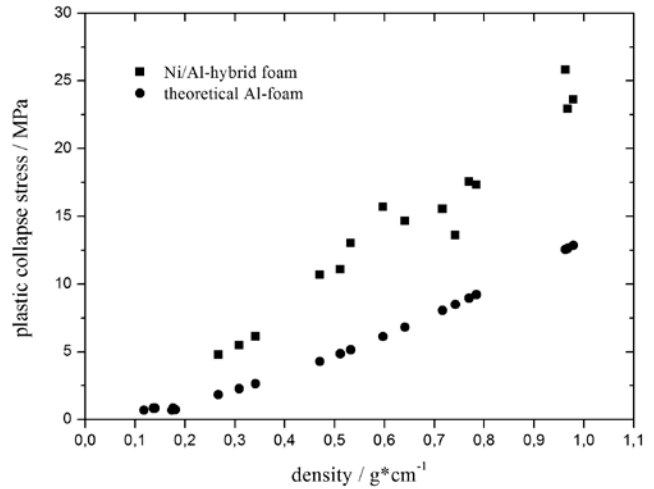


FIG. 14 PLASTIC COLLAPSE STRESS OF NICKEL HYBRID FOAMS AND THEORETICAL ALUMINIUM FOAMS WITH THE SAME DENSITY

The comparison of the energy absorption capacity per density is shown in Fig. 15. Also in this case, the nickel hybrid foams have a much better performance than the theoretical aluminium foams with the same density.
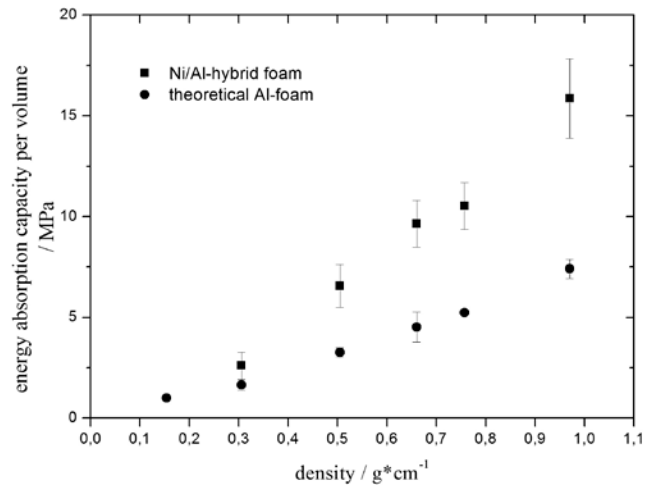


FIG. 15 ENERGY ABSORPTION CAPACITY PER VOLUME OF NICKEL HYBRID FOAMS AND THEORETICAL ALUMINIUM FOAMS WITH THE SAME DENSITY

According to the bending dominated failure mechanism of the pure aluminium foams, there is a quadratic dependency of the energy absorption capacity by the density. The nickel hybrid foams show a linear dependency. This outlines that the predominate failure modes during the plateau phase for the hybrid foams are bending fracture and inelastic buckling. The energy absorption capacity of the

hybrid foams is also strongly affected by the local stress minimum after the plastic collapse stress. This arises from the delamination [6]-[7], [26] of the coating from the substrate foam. A better adhesion between coating and foam reduces the appearance of the local minimum und hence improves the energy absorption capacity [7].

## Conclusions

In conclusion we have shown that electrodeposition of metal foams strongly depend on mass transport limitations. The use of field scans of the remanente magnetic flux density was a good method to determine the coating thickness distribution of nickel coated foams and gave important results for the evaluation of a mass transport limitation model in a porous foam electrode during direct current plating or pulsed electrodeposition. In contrast to further attempts in the literature [6]-[7] we could demonstrate that a more homogeneous coating thickness distribution for thicker foams can be achieved by using a special cage like anode, an enhanced hydrodynamic electrolyte flow, and the use of low current densities combined with low duty cycles. The mismatch ratio of the coating thickness of the outer struts of the foam and the centre could be reduced of 1.25. As a fact of the electromagnetic shielding of the outer ligaments of the foams it will not be possible to produce foams with a totally homogeneous coating thickness distribution over the complete cross section of thick foams. Further work in this field should be done with different duty cycles to evaluate a more detailed mass transport limitation model with respect to detailed parameter identification.

In quasi-static compression tests, we were able to show the significant increased performance of the nickel hybrid foams not only in comparison to the uncoated aluminium foam substrates but also to theoretical pure aluminium foams having the same density as the hybrid foams. The compression strength and load-bearing capacity, respectively of the hybrid foams arise solely from the coating that forms a network of interconnected, nanocrystalline tubes. But the improvement of the energy absorption capacity results from a complex interaction between the substrate foam structure and the mechanical properties of the nanocrystalline shell.

## REFERENCES

[1] M.F. Ashby, A. Evans, N.A. Fleck, L.J. Gibson, J.W. Hutchinson and H.N.G. Wadley, *Metal Foams: a Design Guide*, Butterworth-Heinemann, Woburn, USA, 2000; p. 1-5.

[2] M. Barrabés, A. Michiardi, C. Aparicio, P. Sevilla, J.A. Planell and F.J. Gil, "Oxidized Nickel-Titanium Foams for Bone Reconstructions: Chemical and Mechanical Characterization", *J. Mater. Sci: Mater. Med.* 18, pp. 2123-2129, 2007.

[3] J. Banhart, J. Baumeister, and M. Weber, "Offenporige Aluminiumschäume – Eigenschaften und Anwendungen", *Aluminum*, 75(12), pp. 209, 1994.

[4] J. Banhart, "Manufacturing, Characterization and Application of Cellular Metals and Metal Foams", *Prog. Mater. Sci.*, 46(6), pp. 559-632, 2001.

[5] M.D. Demetriou, J.S Harmon, W.L. Johnson, and C. Veazey, "Amorphous Metal Foams as a Property-matched Bone Scaffold Substitute", WO/ patent 2008/021358, Feb. 21, 2008.

[6] B. Bouwhuis, J. McCrea, G. Palumba and G. Hibbard, "Mechanical Properties of Hybrid Nanocrystalline Metal Foams", *Acta Mater.*, 57(14), pp. 4046-4053, 2009.

[7] Y.C. Boonyongmaneerat, C. Schuh and D. Dunand, "Mechanical Properties of Reticulated Aluminium Foams with Electrodeposited Ni-W Coatings", *Scripta Mater.*, 59(3), pp. 336-339, 2008.

[8] K.J. Euler, "Stromverteilung in und auf Porösen Elektroden", *Chemie-Ing.-Techn..*, 37(6), pp. 626-631, 1965.

[9] A. Jung, H. Natter, S. Diebels, E. Lach, R. Hempelmann, "Nanonickel Coated Aluminum Foam for Enhanced Impact Energy Absorption", *J. Adv. Eng. Mater.*, 13, pp. 23-28, 2011.

[10] H. Natter, M. Schmelzer and R. Hempelmann, "Nanocrystalline Nickel and Nickel-Copper Alloys: Synthesis, Charcterization, and Thermal Stability", *J. Mater. Res.*, 13, pp. 1186-1197, 1998.

[11] H. Natter and R. Hempelmann, "Tailor-made Nanomaterials Designed by Electrochemical Methods", *Electrochim. Acta*, 49, pp. 51-61, 2003.

[12] A. Jung, H. Natter, R. Hempelmann and E. Lach, "Nanocrystalline Alumina Dispersed in Nanocrystalline Nickel: Enhanced Mechanical Properties", *J. Mat. Sci.*, 44, pp. 2725-2735, 2009.

[13] C.H. Hamann and W. Vielstich, *Elektrochemie*, Weinheim, Wiley-VCH, 2005; p 191.

[14] R.C. Sisk and A.J. Helton, "Scanning Instrumentation for Measuring Magnetic Field Trapping in High $T_c$ Superconductures", *J. Rev. Sci. Instrum.*, 64, pp. 2601-2603, 1993.

[15] W. Xing, B. Heinrich, H. Zhou, A.A. Fife and A.R. Cragg, "Magnetic-Flux Mapping, Magnetization, and Current Distribution of $YBa_2Cu_3O_7$ Thin-Films by Scanning Hall Probe Measurements", *J. Appl. Phys.*, 76, pp. 4244-4255, 1994.

[16] D.A. Cardwell, M. Murakami, M. Zeisberger, W. Gawalek, R. Gonzalez-Arrabal, M. Eisterer, H.W. Weber, G. Fuchs, G. Krabbes, A. Leenders, H.C. Freyhardt, X. Chaud, R. Tournier and N. Hari Babu, "Round Robin Measurements of the Flux Trappping Properties of Melt Processed Sm-Ba-Cu-O Bulk Superconductors", *Physica C*, 412, pp. 623-632, 2004.

[17] C. Christides, I. Panagiotopoulos, D. Niarchos and G. Jones, , *Sensors and Actuators A*, 106, pp. 243-245, 2003.

[18] A. Jung, H. Natter, R. Hempelmann, S. Diebels, M.R. Koblischka, U. Hartmann and E. Lach, "Study of the Magnetic Flux Density Distribution of Nickel Coated Aluminium foams", *J. Phys.: Conf. Series*, 200, pp. 1-4, 2011. (http://iopscience.iop.org/1742-6596/200/8/ 082011).

[19] B.E. Warren and L.E. Averbach, "The Effect of Cold-Work Distortion on X-Ray Patterns", *J. Appl. Phys.*, 21, 595-599, 1950.

[20] D.J. Balzar, "X-Ray Diffraction Line Broadening – Modelling and Applications to High-$T_c$ Superconductors", *J. Res. Nat. Inst. Stand. Technol.*, 98, pp. 321-353, 1993.

[21] H. Natter and R. Hempelmann, "Nanocrystalline Copper by Pulsed Electrodeposition: The Effects of Organic Additives, Bath Temperature, and pH", *J. Phys. Chem.*, 100 (50), pp. 19525-19532, 1996.

[22] K. Fischbeck and E. Einecke, *Z. Anorg. Allg. Chem.*, 148, pp. 97, 1925.

[23] J.J. Coleman, *Trans. Electrochem. Soc.*, 90, pp. 545, 1951.

[24] E.O. Hall, "The Deformation and Aging of Mild Steel. 3. Discussion of results", *Proc. Phys. Soc. London B*, 64, 747-753, 1951.

[25] L.J. Gibson and M.F. Ashby, *Cellular solids*, 2nd ed., Cambridge University Press, 1997.

[26] P. Thornton and C. Magee, "Deformation of Aluminium Foams", *Metall. Trans. A*, 6(6), pp. 1253-1263, 1975.